BRNO UNIVERSITY OF TECHNOLOGY
VYSOKÉ UČENÍ TECHNICKÉ V BRNĚ

FACULTY OF INFORMATION TECHNOLOGY
FAKULTA INFORMAČNÍCH TECHNOLOGIÍ

DEPARTMENT OF COMPUTER GRAPHICS AND MULTIMEDIA
ÚSTAV POČÍTAČOVÉ GRAFIKY A MULTIMÉDIÍ

PHOTOMETRIC STEREO PROCESSING FOR MICROSCOPY
FOTOMETRICKÉ STEREOZPRACOVÁNÍ PRO MIKROSKOPY

BACHELOR'S THESIS
BAKALÁŘSKÁ PRÁCE

AUTHOR　　　　　　　　　　　　　　　　　**SAMUEL REPKA**
AUTOR PRÁCE

SUPERVISOR　　　　　　　　　　**Prof. Dr. Ing. PAVEL ZEMČÍK,**
VEDOUCÍ PRÁCE

BRNO 2021

Department of Computer Graphics and Multimedia (DCGM)   Academic year 2021/2022

Bachelor's Thesis Specification

Student: **Repka Samuel**
Programme: Information Technology
Title: **Photometric Stereo Processing for Microscopy**
Category: Image Processing

Assignment:

1. Prostudujte literaturu a další podklady pro více-segmentový detektor SEM používaný v elektronové mikroskopii, kde dílčí segmenty detektoru zobrazují odlišnou intenzitu odraženého signálu podle vlastností povrchu.
2. Prostudujte možnosti zjištění sklonu povrchu v závislosti na odlišnosti lokální intenzity zjištěné jednotlivými segmenty detektoru s tím, že účelem zjištění sklonu je rekonstruovat a vizualizovat topografii povrchu, a to s využitím zjištěného sklonu (prostorového úhlu normály) lokálního místa povrchu preparátu na základně znalosti jasu jednotlivých segmentů detektoru.
3. Navrhněte možnosti kalibrace SEM systému pro zjišťování sklonu, například s využitím preparátů s cínovými kuličkami a diskutujte vlastnosti a možnosti navrženého postupu.
4. Navrhněte a experimentálně implementujte postup rekonstrukce povrchu preparátů ze zjištěných dílčích sklonů preparátů.
5. Diskutujte dosažené výsledky a možnosti pokračování práce.

Recommended literature:

- Image enhancement, 3D reconstruction & metrology software for Scanning Electron Microscopes (2015 MountainsMap SEM): https://doi.org/10.1117/12.7972479 https://www.digitalsurf.com/wp-content/uploads/2018/06/MountainsMap-SEM-7-2.pdf
- Dále dle pokynu vedoucího práce

Requirements for the first semester:

- Body 1 až 3 zadání.

Detailed formal requirements can be found at https://www.fit.vut.cz/study/theses/

Supervisor: **Zemčík Pavel, prof. Dr. Ing.**
Head of Department: Černocký Jan, doc. Dr. Ing.
Beginning of work: November 1, 2021
Submission deadline: May 11, 2022
Approval date: November 3, 2021

Abstract

This paper proposed a method of 3D reconstruction of scanning electron microscope (SEM) specimen. The aim is to explore the possibilities of topography reconstruction of microscopic samples, as well as to attempt to solve the task using tools already available on conventional scanning electron microscopes. The proposed solution uses images from a four-segment backscattered electrons detector as an input to the photometric stereo algorithm. This algorithm exploits the fact that the brightness of the image point is dependent on the inclination of the sample surface. Reflectance maps are used to estimate the inclination in each pixel, creating a map of normal vectors. The map is then used for topography reconstruction. A novel technique for reflectance map estimation is proposed. This method is applied to tin samples to remove the sample's atomic number effects. The fact that all data are acquired simultaneously allows for fast reconstruction. Usage of already available and widespread tools eliminates a need for specialized equipment such as Atomic Force Microscopes.

Abstrakt

Táto práca popisuje metódu 3D rekonštrukciu modelu vzorky pomocou skenovacieho elektrónového mikroskopu (SEM). Obsahuje zhrnutie prístupov k rekonštrukcii topografie a implementáciu algoritmu založeného na princípe fotometrického sterea. Vstupom tejto metódy sú obrazy zo 4-segmentového detektora spätne odrazených elektrónov. Metóda využíva závislosť intenzity jasu na náklone povrchu. Pre odhad náklonu na mieste povrchu sa používajú odrazové mapy, pomocou ktorých sa vytvorí mapa normálových vektorov povrchu. Následne sa z tejto mapy vytvorí 3D model vzorky. Práca predstavuje nový prístup k odhadovaniu odrazových máp. Metóda je aplikovaná len na cínové vzorky, aby sa odstránila závislosť na atómovom čísle materiálu. Všetky dáta potrebné pre algoritmus su získané simultánne, čo umožňuje rýchlu rekonštrukciu. Algoritmus používa rozšírené a existujúce nástroje, čím umožňuje rekonštruovať povrch bez špecializovaných nástrojov.

Keywords

Photometric stereo, Scanning electron microscopes, 4-segment BSE detector, 3D reconstruction

Klíčová slova

Fotometrické stereo, skenovacie elektrónové mikroskopy, 4-segmentový detektor spätne odrazených elektrónov, 3D rekonštrukcia

Reference

REPKA, Samuel. *Photometric Stereo Processing for Microscopy*. Brno, 2021. Bachelor's thesis. Brno University of Technology, Faculty of Information Technology. Supervisor Prof. Dr. Ing. Pavel Zemčík,

Rozšířený abstrakt

Skenovacie elektrónové mikroskopy sú neoddeliteľnou súčasťou súčasnej vedy. Poskytujú množstvo informácií o povrchu vzorky, a to nie len o jej vzhľade, ale aj o chemickom zložení, kryštalickej štruktúre, elektrických vlastnostiach a podobne. Čoho ale tieto mikroskopy schopné nie sú, je ukázanie vzorky v priestore, teda 3D zobrazenie. Táto práca sa venuje riešeniu tohoto problému pomocou metódy známej ako fotometrické stereo, kde na vstupe do algoritmu je skupina snímiek, ktoré sú získané z rovnakého uhla pohľadu, ale zakaždým v iných "svetelných" podmienkach. Táto metóda je známa už viac ako 40 rokov, ale jej aplikácia v kontexte skenovacích elektrónových mikroskopov nie je veľmi rozšírená. To je z veľkej časti spôsobené aj netriviálnou problematikou závislostí na nastaveniach mikroskopu, ako napríklad urýchľovacieho napätia, elektrónového prúdu alebo pracovnej vzdialenosti. Odrazové charakteristiky elektrónov sú ovplyvnené aj samotným chemickým zložením vzorku a v neposlednom rade aj internými nastaveniami mikroskopu. Hojnosť premenných, s ktorými musí algoritmus kalkulovať, viedla k rozhodnutiu obmedziť kalibráciu na cínové vzorky a konštantné nastavenia detektoru.

V tejto práci sa využíva 4-segmentový detektor spätne odrazených elektrónov, ktorého segmenty sú symetricky usporiadané okolo elektrónového lúča. Každý zo segmentov sníma vlastný signál a teda vyprodukuje vlastnú snímku. Výsledné 4 snímky sa javia ako získané z rovnakého uhla pohľadu, a s osvetlením ktoré rotuje o 90 stupňov, teda sú presne splnené podmienky fotometrického sterea. Na zistenie náklonu povrchu v každom bode z týchto štyroch obrázkov sa používajú odrazové mapy, ktoré mapujú intenzitu odrazeného žiarenia (v princípe teda hodnotu pixelu) na jednotlivé náklony povrchu. Jedna z nových myšlienok v tejto práci je aproximácia týchto odrazových máp pomocou superelíps.

Navrhnutý algoritmus je trojkrokový. V prvom kroku sa odhadne odrazová mapa na základe nastavení mikroskopu v čase snímania. V tejto metóde sa používa aproximácia empiricky odvodených vzťahov pomocou interpolačných kriviek. Druhý krok je počítanie náklonov povrchu v každom bode snímiek, výsledkom ktorého je mapa normálových vektorov povrchu. Tretí krok je samotná 3D rekonštrukcia zo získanej mapy normálových vektorov.

Algoritmus bol implementovaný a testy ukázali, že je schopný rekonštruovať povrchy vzoriek spadajúcich do kalibračného rozmedzia s dobrou presnosťou. Implementácia bola otestované aj na vzorkách, pre ktoré progam kalibrovaný nebol a s menšími úpravami bol schopný odhadnúť probližné tvary vzorky. V tom prípade sa ale naozaj jednalo iba o odhad. Stanovené ciele teda boli splnené a ukázalo sa, že rekonštrukcia pomocou empiricky odvodených odrazových máp má potenciál.

Photometric Stereo Processing for Microscopy

Declaration

I hereby declare that this Bachelor's thesis was prepared as an original work by the author under the supervision of Mr. Pavel Zemčík. The supplementary information was provided by Mr. Vojtěch Filip. I have listed all the literary sources, publications and other sources, which were used during the preparation of this thesis.

<div align="right">

. . . .

Samuel Repka

May 11, 2022

</div>

Contents

Chapter 1

Introduction

As science progresses, the requirements for data acquisition instruments are increasing. What sufficed in the past, nowadays, is not enough. While optical microscopes provide an excellent tool for viewing the micro and nano world, the fundamental nature of light limits their resolution to about 100nm. That is where electron microscopes made a breakthrough. The electron microscopes are capable of viewing with resolution far below the limit of optical microscopes and acquiring additional data like sample structure, conductivity, and chemical composition. This work aims to expand the capabilities of electron microscopes by adding the ability to reconstruct the sample topography.

Non-destructive topography acquisition of the sample using the scanning electron microscope can be divided into two groups. Photogrammetry is one of them. In this method, numerous images are taken from different angles. Surface features are then determined by finding shared points on the images and calculating distances between them.

The second approach is called photometric stereo, which is the main focus of this thesis. The topography is estimated from multiple sample images, where each image is taken approximately from the same place but under different „lighting" conditions. The images originate from the four-segment back-scattered electrons detector. Although this approach is not new, implementation and usage in the electron microscopy field are lacking. The topic for this thesis was commissioned by the TESCAN company, which supplied data, consultations, and expert knowledge. I chose this topic because of my interest in electron microscopy and the effort to make something useful for the world.

The following chapter explains the basic principles of electron microscopy, a more in-depth description of the scanning electron microscope and backscattered-electron detector, and other knowledge necessary to understand this thesis. The third chapter is an overview of existing approaches to topography acquisition, and the fourth chapter mentions several implementations of the photometric stereo approach. The first part of the fifth chapter assesses the current knowledge and sets goals to be fulfilled with the implementation. Successive parts of the chapter describe implementation decisions, tools, and development data. In the sixth chapter, the specific steps are described and explained. In the last chapters, the evaluation of the criteria set in the fifth chapter can be found, as well as experiments and testing.

Chapter 2

Electron microscopy introduction

Electron microscopes are an inseparable part of today's science. Many fields rely on the instrument as the insight into the nanoworld provides many kinds of information about our own world. Electron microscopes are used in the semiconductor industry [3], life sciences [2], earth sciences [28], materials science [29], and more. This chapter explains the fundamental principles of electron microscopy and other knowledge closely related to this thesis. It is not a comprehensive overview of the topic because of the limited scope of the work.

2.1 Basic principles

The main reason for the development of electron microscopes was the limited resolution of light microscopes caused by the wavelength of visible light. As the electron wavelength is much lower than that of the photons, it has the potential for much better viewing resolution. The resolution limit R is given, for example, by a Rayleigh criterion that is given by

$$R = 0.61 * \frac{\lambda}{NA} \tag{2.1}$$

where λ is the wavelength of the used radiation, and NA is the numerical aperture of the microscope's objective lens [11].
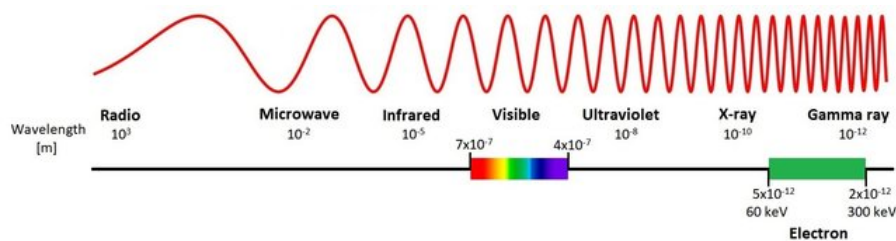

Figure 2.1: Comparison of the different wavelengths of electromagnetic spectrum and accelerated electrons. [1]

Only later the many more uses of the electron microscope were discovered [34]. Electron microscopes use a beam of accelerated electrons to probe the sample. The electrons then interact with the specimen, and the resulting particles are captured and imaged. They are capable of viewing resolution down to 50 picometres [8]. Compared to the highest resolution

---
[1]Image from literature [30].

of the light microscope (100 nm [23]), it is a substantial improvement. Two main types of electron microscopes are Transmission electron microscope (TEM) and Scanning electron microscope (SEM).

The transmission electron microscope is based on the technique in which the electrons pass through the specimen. However, this work focuses on a scanning electron microscope, described in detail in the next section.

2.2   Scanning electron microscopes

The scanning electron microscope uses a focused electron beam to scan the specimen. The electrons emitted from the electron source (electron gun) are then accelerated and shaped by the electrostatic or magnetic lenses to reduce the beam diameter. Other lenses are then used to aim the beam to the specific location on the specimen. The sample is scanned at closely spaced discrete locations in a raster. The electron beam interacts with the surface of the sample, creating various products like backscattered electrons, secondary electrons, Auger electrons, X-rays, and more. Respective detectors then capture the particles, and the signal from them can be digitized, processed and shown on the monitor [13]. These detectors provide data about the crystalline structure, surface topography, chemical composition, and electrical behaviour [31].

Advantages of the scanning electron microscope include a wide range of magnification (up to six orders of magnitude) and simultaneous acquisition of data from different detectors. Sample preparation time can be extremely short since all that needs to be done with a conductive non-oily or non-wet specimen is to attach it to the specimen holder. Data acquisition time lasts from a few milliseconds to several minutes, depending on the desired signal to noise ratio. Scanning with SEM can be non-destructive, unlike TEM, where sample preparation is undoubtedly destructive.

Over the years, the scanning electron microscope branched into many variations. Field Emission Scanning Microscope (FESEM) uses a field-emission gun instead of a thermionic gun. Variable Pressure Scanning Electron Microscope (VPSEM), also known as Environmental Scanning Electron Microscope, can operate in a low vacuum, observing wet or dirty specimens. Scanning Transmission Electron Microscopy (STEM) combines the SEMs and TEMs. Similar to transmission electron microscopes, it requires samples to be sufficiently thin to transmit electrons. The specimen is then scanned in raster, differentiating STEM from the conventional TEM [14].

Electron gun

The electron gun is an electron beam source with adjustable energy and electron current, as seen in Figure 2.2. Because electrons interact with the air particles, which causes unwanted noise in detectors and defocuses beam, it is crucial to keep the electron beam in the vacuum. Typically, the incident beam electrons have energies of 2-40 keV. The source of the electrons can be divided into three categories: thermionic emitters, cold field-emission guns and Schottky emission cathodes.

The filament of the thermionic emitter is heated to a temperature sufficient to overcome the work function of the material. The work function is the minimum energy needed to remove an electron from the surface of the solid. The most common thermionic emitter is

---

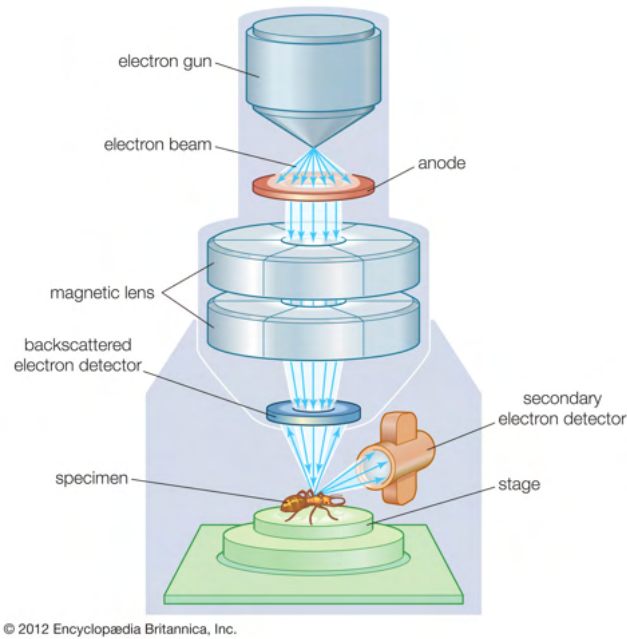[2]Image taken from https://www.britannica.com/technology/scanning-electron-microscope

Figure 2.2: Schematic of scanning electron microscope.[2]

a tungsten hairpin filament. The filament is heated to approximately $2500°C$ to allow for electron emission. Another filament is made out of Lanthanum hexaboride (LaB_6). This material has a lower work function compared to the tungsten filament, and because of it, it features a „brighter beam" and longer lifetime but is more expensive [31].

Schottky emission cathodes are heated to 1000 -1500 K to lower the work function. The high electric field is applied to the cathode, which decreases the potential barrier, causing the emission of the electrons [19]. This is known as the Schottky effect, or field enhanced thermionic emission.

The cold field emission cathodes provide superior beams in brightness and stability of electron energy. Electrons escape the surface of the emitter due to quantum tunnelling, which occurs because of an externally applied electric field [25]. However, they require a much higher vacuum than thermionic guns. This requirement reflects the higher cost of the microscope [31].

Lenses

The electron gun produces a divergent electron beam. In order to focus and aim the beam, electrostatic or magnetic lenses are utilized. Multiple lenses are located in the microscope column. At first, two to three electromagnetic lenses are used to reconverge the electron beam. These lenses are called condenser lenses and are symmetrical. The electron beam then passes through the objective lens, which focuses the beam to the smallest possible spot on the sample surface. The objective lens is asymmetric in order to minimize the magnetic field in the vicinity of the sample.

The lens suffers from many deficiencies, some of which are mentioned here [13] [14].

- **Spherical aberration** - electrons near the optical axis are refracted less significantly than electrons further from the axis

- **Chromatic aberration** - electrons of different energy (wavelength) are focused to the different points

- **Aperture aberration / diffraction** - diffraction on the objective aperture

- **Astigmatism** - aberration caused by various reasons, for example magnetic inhomogenities or dirty lenses

Some aberrations are minimized by careful microscope construction; others heavily depend on the current microscope setup. For example, a greater working distance (distance between the objective lens and the specimen) causes a bigger electron probe diameter [14]. Astigmatism is compensated using stigmators, which are special lenses located usually near the objective lens.

Stage

It is necessary to ensure that the specimen is kept at the ground potential. Otherwise, the charge created on the sample would distort the image. Moreover, the sample usually has to be moved during the scanning process, requiring great precision. The specimen stage does precisely that. The stage can be loaded through the specimen-exchange airlock, or the whole microscope must be vented, and the stage is accessed directly.

The stage allows movement in the x, y and z-axis, rotation around the central microscope column axis, and tilting. Modern stages are motorized.
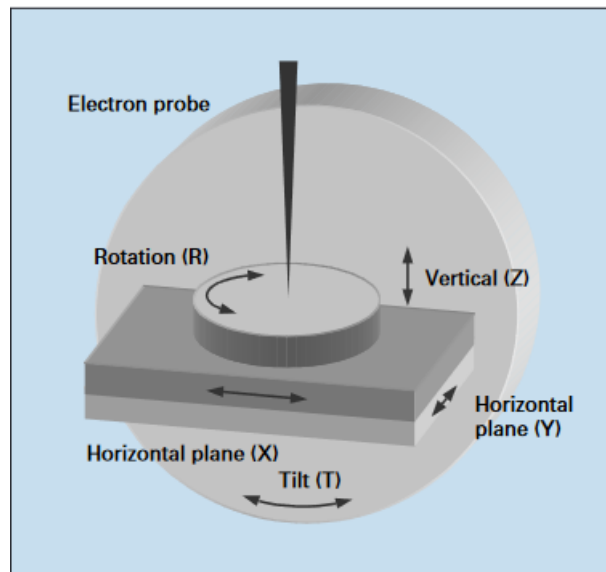

Figure 2.3: Stage construction.[3]

For specific purposes, a special stage is required. For example, hot stages are used to investigate the sample in high temperatures. Cryo or cold stages facilitate research in a cold environment. Deformation stages are used to study specimen deformation, such as bending and compression [14].

---

[3]Image from literature [16].

Detectors

Interactions of the incident beam with the surface specimen yield many byproducts. The physical processes, also known as scattering events, are ways of energy transfer from the impinging electrons to the sample atoms. In the context of Scanning electron microscopes, these interactions are often classified as elastic and inelastic. Because of the energy loss in the sample, the penetration depth of the beam is limited.

When scattering is inelastic, it denotes that the physical process where the primary electron transferred its energy to the specimen took place. An example of the product of inelastic scattering is the secondary electron.

Elastic scattering refers to the process of deflecting the primary electron from its current path by the electrical field. Even though their trajectory is altered, the electron energy remains effectively unchanged. The range of angular deviations is from a few degrees up to 180°. A prime example of an elastic scattering product is a backscattered electron [13].

- **Secondary electrons**
  Secondary electrons originate in the atom itself, knocked out of their orbit by an electron from the beam. Their energy is below 50 eV [31]. Because of their low energy, only secondary electrons from the shallow layer on the surface are observable. This depth is called escape depth and is dependent on the atomic number of the elements. It is about 5 nm for metals and 75 nm for insulators [14]. They provide topographic information, as well as some information about specimen composition.
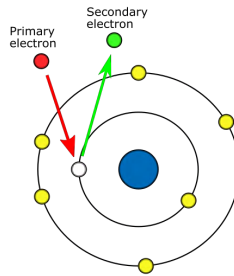

Figure 2.4: Secondary electrons

- **Backscattered electrons**
  Incident beam electrons that undergo scattering events that reverse their trajectory and leave the sample are called backscattered electrons. By definition, the energy of the backscattered electrons is higher than 50 eV and lower or equal to the energy of the impinging electrons. They provide much information about the specimen, such as chemical composition, topography, and crystallography.

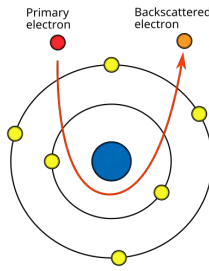 *This type of electrons is described in detail in the next section.*

Figure 2.5: Backscattered electrons

- **X-Rays**
  When the inelastic scattering occurs, the atom is left with a vacancy in the electron shell. This vacancy can be filled by an electron from the higher-level shell, provided it exists. For example, a vacancy in the K shell would be filled with an electron from the L shell. The energy difference can be manifested in two ways. It can be transferred to the other electron, ejecting it and creating a so-called Auger electron, or the X-ray photon can be formed, carrying away the inter-shell transition energy [13]. X-rays provide information about the chemical composition of the sample.
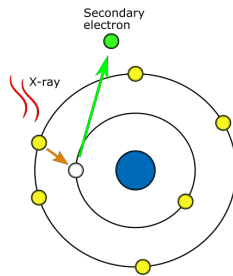

Figure 2.6: X-Rays

- **Auger electrons**
  Auger electrons are created as an alternative product of filling the vacancy after the inelastic scattering occurs. An electron from the higher-level shell fills the vacancy, and the energy difference is transferred to another electron, which is then ejected from the shell with a specific energy. Same as X-rays, they provide information about the chemical composition of the sample surface [13].

Drawbacks

Scanning electron microscopes are cutting-edge technology. Even though the instrument is very versatile, some conditions must be met in order to acquire an accurate measurement. For example, electron microscopes require a vacuum in the scanning chamber. The vacuum is necessary because of the potential interactions between electrons in the beam and air molecules. The air would also cause unwanted scattering of the electron beam [13]. The vacuum is the reason why it is challenging to observe wet or oily specimens with the SEM, as the liquid would evaporate into the chamber.

Because the electron beam delivers electrons to the sample, draining of the said electrons must be ensured. If the specimen is not conductive by itself, other discharging methods have

to be used, e.g. conductive coating of the specimen or usage of a low-vacuum chamber. The chamber is filled with gas that does not intervene with the electron beam but provides sample discharging. If the sample is not grounded, it becomes charged, significantly decreasing the accuracy of the measurements [31] [15].

SEMs are considered to be non-destructive, but some damage to the sample does occur. The chemical bonds can be broken because the specimen is ionized with the electron beam. The excited species will then recombine, sometimes forming new structures. In crystalline materials, this leads to the breaking of the crystal structures. Moreover, the specimen is subject to contamination with hydrocarbons. The hydrocarbons can originate in the microscope itself (e.g. from vacuum grease) or the specimen (e.g. atmospheric molecules bound to the sample) [14].

2.3 Backscattered electrons and BSE detector

As previously stated, the backscattered electrons are the product of scattering events, both elastic and inelastic. [7] By definition their energy is above 50 eV. Not every electron from the beam becomes a backscattered electron. Some electrons are entirely absorbed in the specimen or can even penetrate the sample, becoming transmitted electrons. That is why the term „backscattered electron coefficient" was introduced.

Backscattered electron coefficient

Backscattered electron coefficient η quantifies fraction of incident electrons that become bacscattered electrons. It is defined as

$$\eta = N_{BSE}/N_B \tag{2.2}$$

N_B is the number of impinging electrons, whereas N_{BSE} is the number of backscattered electrons.

The backscattered electron coefficient is dependent on **the atomic number** of the elements of the specimen. Elements with higher atomic numbers backscatter more electrons. The Monte Carlo method is often used when simulating scattering events in the specimen. For the demonstration purposes, simulations using CASINO simulation tool [5] were made, where the behaviour of the electrons is seen.
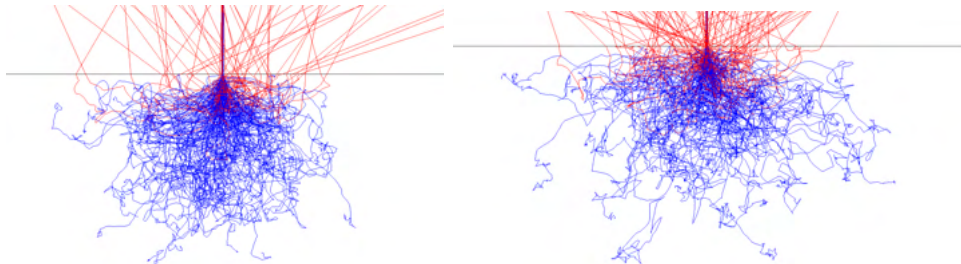

Figure 2.7: Monte Carlo simulation - blue lines are paths of the absorbed electrons, red lines are paths of the backscaterred electrons. The sample is a bulk copper.

Different backscattering coefficient for different elements is reason, why the composition contrast is present in the sample scans. Figure 2.8 demonstrates such composition constrast.
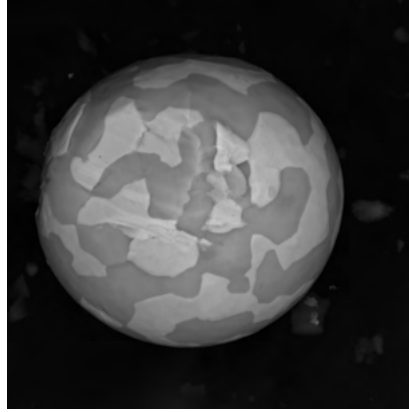
Figure 2.8: Solder ball with different elements visible. Brighter material is lead, darker one is tin.

The inclination of the surface also influences the η. Simulation shows that greater inclination causes a significant increase in the measured backscattered coefficient. This effect can be used to reveal sample topography; however, the BSE detector with a large collection angle has to be used. Detectors with a small collection angle may not capture this contrast because of the angular distribution of backscattered electrons [13].

Angular distribution of the BSE

The energy of the incident electrons, incident angle and material of the sample heavily influence the angular distribution of the BSE. Generally, the distribution consists of two parts. One is made out of electrons diffusely scattered throughout the material, which can be approximated by Lambert's distribution. The second one consists of electrons originating in smaller exit depth. This second part exhibits „reflection-like" properties. At an incidence angle of 0°, the „reflection-like" component of the distribution is negligible. However, the greater the angle, the more prominent the „reflection-like" component of the distribution is. [24] The polar diagrams in Figures 2.9, 2.10, 2.11 show dependencies of angular distribution $d\eta/d\Omega$ on various incident angles, energies and materials. η is a backscattering coefficient, and Ω is a solid angle, explained in the Subsection 2.3.
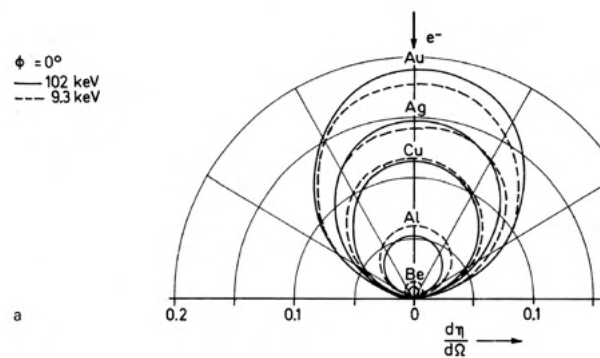

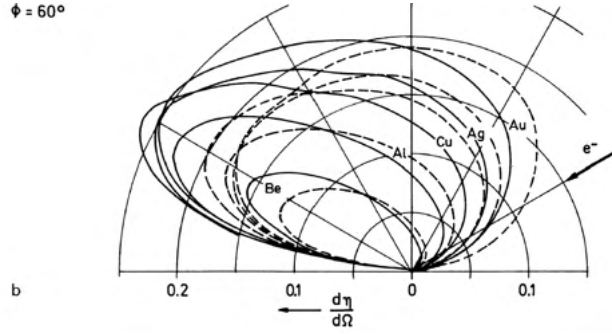Figure 2.9: At incidence angle of 0°, the circular shape can be approximated with Lambert's cosine law. [24].

Figure 2.10: Polar diagram of the BSE distribution for various elements and electron energies at incidence angle of 60°. [24].
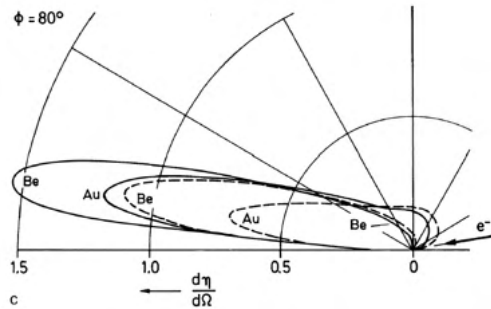

Figure 2.11: Polar diagram of the BSE distribution for various elements and electron energies at incidence angle of 80°. The Au at 9.3 keV shows a large diffusely scattered component of the distribution. [24].

BSE detectors

Because of the relatively high energy of the BSE, they can be captured directly without additional acceleration. This property puts most BSE detectors into the category of *passive detectors* [13]. An important property of the detector is the solid angle Ω. It is calculated as

$$\Omega = A/r^2 [sr] \tag{2.3}$$

When compared to the solid angle of the hemisphere, it tells us an estimate of overall geometric efficiency [13]. Figure 2.12 shows that even though the detector D_2 has a much more extensive collection area, the solid angle is similar to that of the D_1 because of the distance from the sample.

Mainly two principles are employed to detect BSE. One of them utilizes the scintillation materials to convert electrons to photons, which are then converted to the electric signal by a photomultiplier.

The latter uses semiconductors to detect the BSE. The impinging backscattered electrons generate electron-hole pairs. The recombination can be prevented by applying an appropriate electrical field, and generated electrons can be then collected. The measured current is then proportional to the number of impinging BSE. [14]

- **Everhart-Thornley (ET) detector** - The most common detector in the scanning electron microscopes. It features the capability to detect both secondary electrons
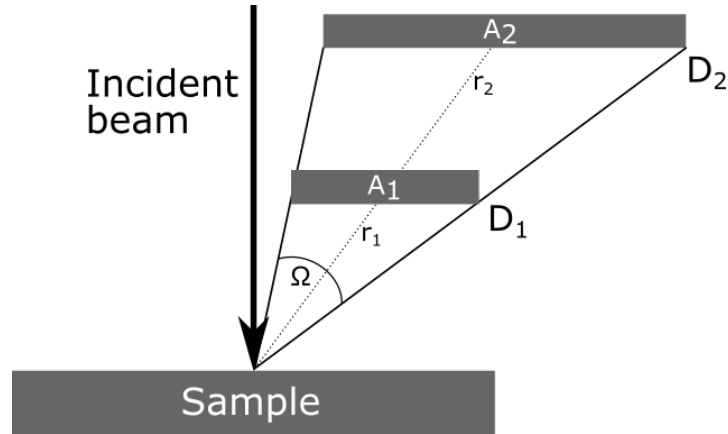
11

Figure 2.12: Solid angle - Despite detector D_2 being much larger than detector D_1, the solid angle Ω is the same due to the D_1 being closer to the sample.

and backscattered electrons. In the front of the detector is the collector grid with selectable potential that ranges from about -50 to 300V [13]. When the grid is positively biased, both secondary and backscattered electrons are collected. Negative bias on the collector grid causes secondary electrons to be repelled. However, it is not enough to stop the backscattered electrons, causing the detector to collect just BSE heading directly towards the detector. Captured electrons are then accelerated because secondary electrons have too low energy to be detected. The accelerated electrons then hit a scintillator, which converts them to the photons that are converted back to the electrons through the photomultiplier. The output from the photomultiplier can be amplified further. [14]

- **Microchannel plate detector** - An unconventional detector for SE and BSE with a tiny footprint. It is designed to be fitted on the final lens of the pole piece. The detector consists of many parallel tubes of size 10-20 μm. The electrons entering these tubes are multiplied, yielding electron gains of approximately 1000 orders. The detector is efficient even at accelerating voltages below 1 keV [21].

- **4-segment semiconductor detector** - Many designs of semiconductor detectors exist, one of which is the 4-segment detector. It consists of four separate detectors, symmetrically placed around the incident beam as seen in Figure 2.13.

  Each segment captures backscattered electrons from different locations, causing the specimen to be seen as if under different lighting conditions. Acquisition of all four images is simultaneous, meaning only a single scan is required to acquire data from all segments. These properties make the detector ideal for applying photometric stereo, which is why it is used further in this thesis.

  Different combinations of images emphasize different properties. For example, the summing of all four images brings out the composition of the specimen, whereas subtracting emphasizes topography.

Various detectors have various settings in order to broaden the detection range or manipulate the output signal to be appropriate for A/D converters. Two such settings are the gain and the offset. The gain is a multiplication operation of an input signal with a given
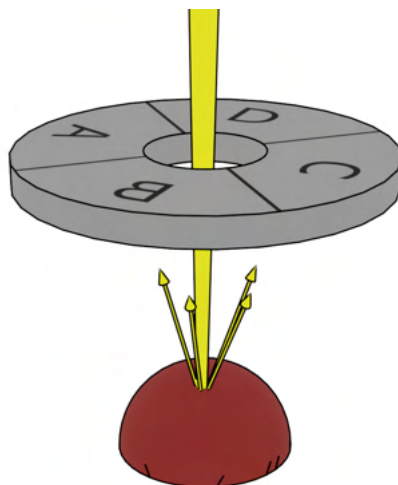
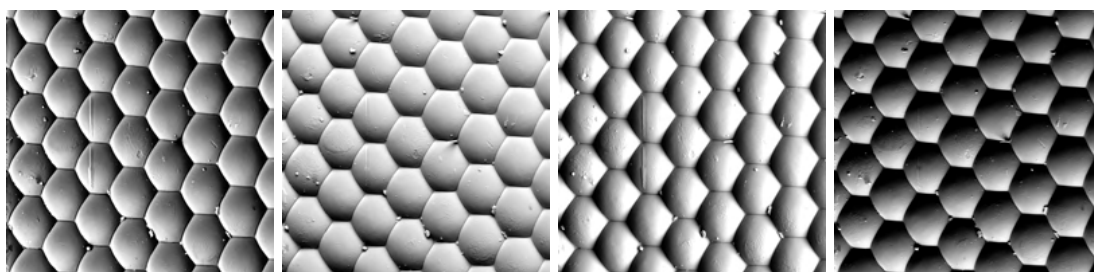Figure 2.13: Schematic of the BSE detector

Figure 2.14: 4 images of the same eye of the fly, but each image is from different segment of the detector.

constant. On the other hand, offset is adding a constant to the input signal. Together, these two operations can be written as:

$$s_o = a * s_i + b \tag{2.4}$$

where s_i and s_o are input and output signals respectively, a is a gain coefficient and b is an offset coefficient.

Chapter 3

Approaches to the topography reconstruction

While there is no native solution to acquire a 3D model of the sample using SEM, there are methods, equipment, or special procedures that allow for the measurement of the sample topography. This chapter lists some of the approaches chosen to illustrate the variability in possible solutions and provides an introduction to the photometric stereo method used in this work. Note that this is by no means a complete list of available methods.

3.1 Photogrammetry

The American Society for Photogrammetry and Remote Sensing (ASPRS) [20] defines photogrammetry as follows:

> „Photogrammetry is the art, science and technology of obtaining reliable information about physical objects and the environment through processes of recording measuring and interpreting images and patterns of electromagnetic radiant energy and other phenomena.“

There are two types of photogrammetry, metric and interpretative photogrammetry. Metric photogrammetry, in general, is about determining the relative locations of points in the images. Subsequently, additional information can be found like volumes, angles, surfaces, etc. Interpretative photogrammetry concerns recognizing, identifying, and evaluating objects on the images. [36] Given the nature of this work, further mentions of photogrammetry will relate to metric photogrammetry.

Photogrammetry found its use in many fields, such as cartography, where it is used to create maps, astronomy, architecture, archaeology, ecology, oceanography, and many more. Nowadays, the use of photogrammetry exceeded the boundaries of laboratories and specialized equipment. Conventional smartphone camera, in combination with the software of choice, allows for creating amateur 3D models.

The first step of 3D reconstruction is acquiring multiple images of the required scene. The photos have to be taken from different points of view. The photogrammetry algorithm uses these photos, and by using various triangulation algorithms calculates subject geometry. A sufficient number of distinct points must be provided, as the algorithm relies on these points throughout the computation [10]. An example of such an algorithm is shown in Figure 3.1.
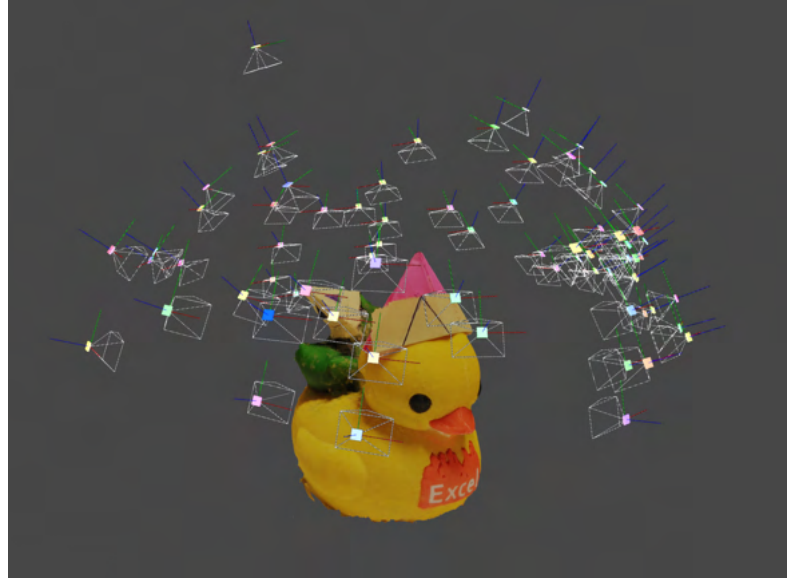
Figure 3.1: A 3D render of the model acquired by means of photogrammetry. The image was reconstructed from 71 photos with the free open-source software Meshroom 2021.1.0. Note that when the ducks did not have hats, the algorithm was not able to reconstruct the 3D model, as there were not enough distinct points on the images.

Photogrammetry and SEM

It has been proven that the application of photogrammetry to the topography reconstruction of SEM micrographs is a viable option [9]. Because of the inability to move detectors inside of SEM, the specimen with the stage is rotated. Several overlapping images are acquired, stitched together, and processed by conventional photogrammetry software. Significant advantages of this method are that it is non-destructive and relatively fast.

However, the method has some limitations. It requires a specimen to be stable for the acquisition time and is susceptible to failure if the sample has too complex of a surface or no distinctive features.

3.2 Atomic force microscopy

Yet another take on visualizing surface microfeatures, atomic force microscopy, is a well-established field in today's science. Atomic force microscopes (AFM) utilize physical touch to sense the height of the sample point. The main parts of the AFM are the extremely sharp tip (used to touch the sample surface), force sensor (for sensing the force between the tip and the sample), sample holder, and mechanism for moving the tip. The tip is moved over the sample surface in a raster pattern in the x and y axes. The movement on the Z-axis is controlled by feedback control. The feedback control principle is that the AFM tries to maintain the force between the tip and the sample. If the force sensor detects increased values, surface features have „pushed" onto the tip, raising it to maintain the force. Similarly, if a drop in the contact force is detected, the tip is lowered. This motion is measured, and topography is acquired.

AFM can achieve incredible resolution, even down to 0.1 nm in x-y axes and sub-angstrom resolution in z-axis [6]. Although originally developed for topography measure-
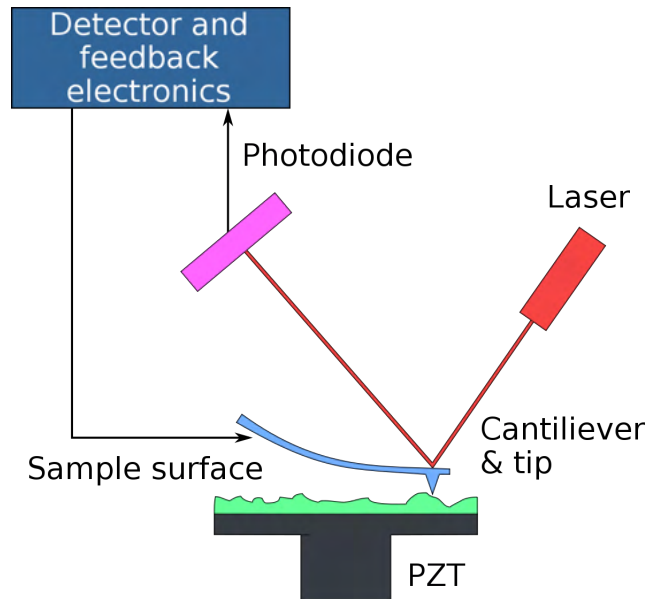
Figure 3.2: Schematic of the atomic force microscope.

ment, modern AFMs are capable of investigating more features, for example, magnetic and electrical properties of the specimen. In addition to being non-destructive, AFM allows examining both conductive and non-conductive samples without special preparation, outside the vacuum, and at various temperatures.

Scanning of bigger samples ($> 100\mu m$) can be very time-consuming, as the tip of the AFM needs to traverse the whole sample surface. The quality of the measurement depends on the sharpness of the tip; if the tip is dull, the resolution drops.

3.3 FIB-SEM 3D imaging

Focused ion beam (FIB) is a technology very similar to SEM. However, FIB uses an ion beam, most often Gallium ions, instead of an electron beam, allowing for some unique capabilities, e.g., machining the sample. Because of the relatively high kinetic energy of the ions, the interactions of the beam and sample surface include sputtering (removing of atoms) and ion emission. Effectively, it is possible to „dig" into the sample with FIB. Moreover, in combination with a gas injection system (GIS), deposition of atoms onto the specimen is possible. FIB is most frequently used for TEM sample preparation, microstructural analysis, and nanomachining [32].

FIB can be integrated into the SEM to create a dual-beam platform where both FIB and SEM columns are present (see Figure 3.3). This enables the use of the SEM for observation of the specimen before, during, and after preparation using FIB. This system can be used to perform microstructural tomography. The ion beam is used to remove layers of the sample. The layers can be thinner than 10 nm [39]. After each removal, the new surface is imaged using SEM. After the acquisition, the imaged layers are processed, and a 3D model is created. With some preparations, microtomography can be used to reveal the topography of the specimen surface [40].

This method is very accurate and is able to surpass even the accuracy of the Atomic force microscopes. It allows for the investigation of not only the surface but also of the
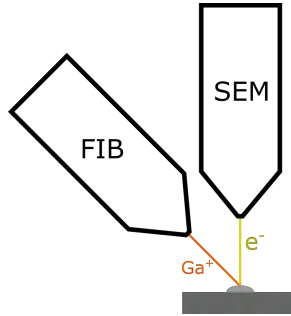
16

Figure 3.3: Schematic of the dual-beam instrument. Gallium ions were chosen just for demonstration purposes.

internal structures. However, it is not applicable to the samples with high surface roughness, as the surface needs to be covered entirely in the secondary material [40]. This method is very time-consuming because sample preparation, subsequent milling of the layers, and imaging can take days or even weeks [39]. The method is also destructive, making the sample unsuitable for further examination.

3.4   Shape-from-shading and photometric stereo

Both shape-from-shading and photometric stereo are methods of computing of 3D surface shape from the image brightness [22]. They do not provide a 3D model of the surface directly but a map of surface normals. The map can be further processed to acquire a 3D model. While the shape-from-shading approach works with only one grayscale image of the scene, photometric stereo utilizes data from multiple grayscale images.

The shape-from-shading problem is an especially difficult one because of the small amount of data available. When the problem has been formulated by Horn [35] as a resolution of a non-linear first-order Partial Differential Equation (PDE), called the brightness equation [22]. It has been proven that the solution of such a task is not unique [18]. Given these difficulties, various assumptions are usually made in order to reach an approximate solution, such as orthographic camera projection or calibrated light conditions [26].

Photometric stereo uses multiple images to determine the surface inclination. What differentiates it from the photogrammetry is the fact that all images are taken from a single point of view, but the position of the source of light changes (Figure 2.14). This way, there is no need to find a relation between the images, as it is implicit. Woodham [37] proposed the usage of reflectance maps to find a normal in a point. To understand what a reflectance map is, one must comprehend a gradient space.

Gradient space

Assume an orthographic projection of a surface explicitly defined as a function of its coordinates $z = f(x, y)$. The viewing direction is aligned with the negative z-axis, and the x and y coordinates of the projection correspond to the coordinates of the surface. With these assumptions, a surface normal can be represented by a vector of its partial derivatives with respect to x and y.

$$\left[\frac{\partial f(x,y)}{\partial x}, \frac{\partial f(x,y)}{\partial y}, -1 \right] \tag{3.1}$$

After defining parameters p and q to be

$$p = \frac{\partial f(x, y)}{\partial x} \tag{3.2}$$

$$q = \frac{\partial f(x, y)}{\partial y} \tag{3.3}$$

the vector of the surface normal can be rewritten as a $[p, q, -1]$. *Gradient space* is a two-dimensional space representing the inclination of every surface point, defined on p and q. The space itself is infinite, as derivatives of possible inclinations approach infinity in the extremums [37].

Reflectance map

Reflectance map defined in gradient space determines reflectance of the surface for a given object material, light source, and viewer geometry [37]. Such a reflectance map can be derived analytically, for example, with the bidirectional reflectance distribution function, or determined empirically. In Figures 3.4 and 3.5 reflectance maps are represented as a series of iso-brightness contours in the gradient space.
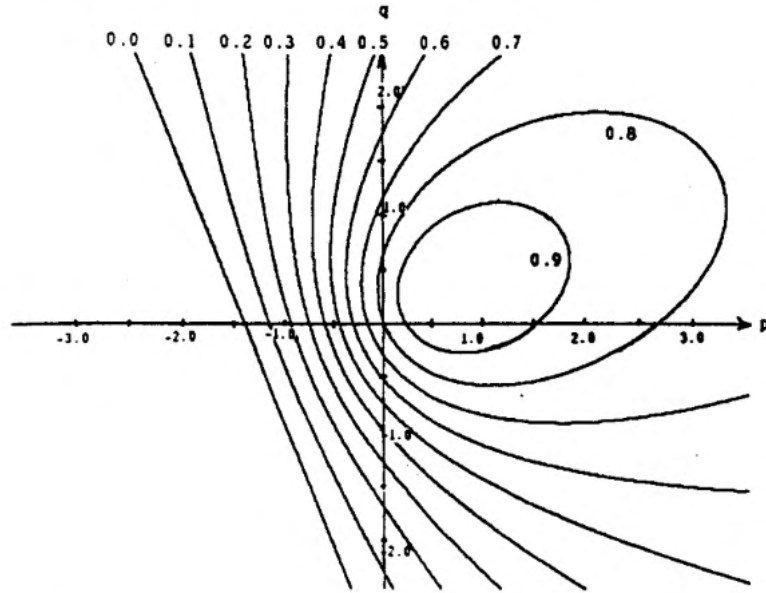

Figure 3.4: The reflectance map R(p,q) for a lambertian surface illuminated from gradient point $p_s = 0.7$ and $q_s - 0.3$. The reflectance map is plotted as a series of contours spaced 0.1 units apart.[1]

Having multiple images with different illumination assures that their reflectance maps are not the same. Two images would suffice to determine a surface normal uniquely, provided that the reflectance maps are linear. However, that may not be the case, as seen in Figure 3.4. Sometimes more than two images are necessary to find the solution. Assuming the knowledge of the reflectance maps, the reaching of the solution is much simpler compared to the shape-from-shading method.
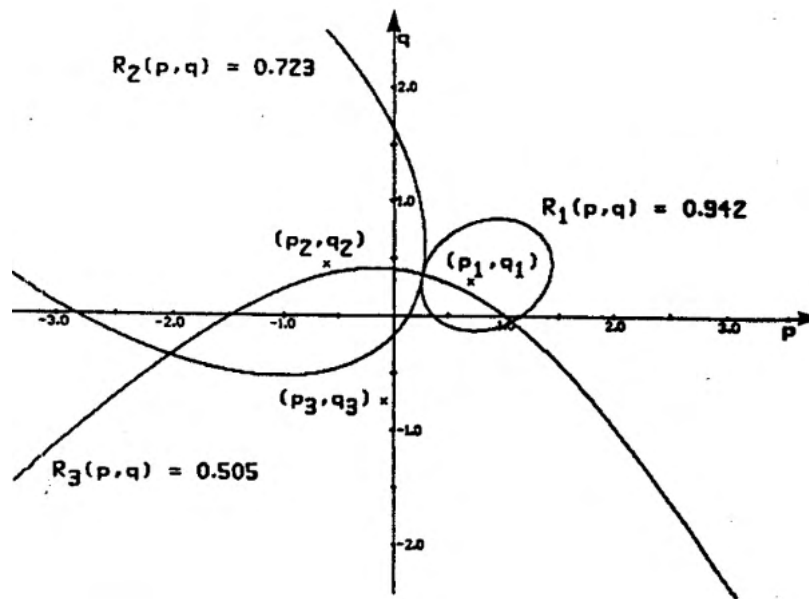
---

[1]Image taken from the literature [37].

Figure 3.5: An example of uniquely determined surface orientation. Three contours were overlayed through one another, each contour originating from a different reflectance map. The contours were obtained by selecting intensities of the same point (x,y) from separate images.[2]

Photometric stereo has been researched for more than 40 years. Many solutions were invented; however, most of them were made for surfaces illuminated with light. In this thesis, a photometric stereo problem is being solved with the help of reflectance maps acquired empirically. For this reason, other methods of photometric stereo are not described here.

---

[2]Image taken from the literature [37].

Chapter 4

Avaliable commercial solutions

This chapter is an overview of some of the existing solutions available. Sometimes, 3D reconstruction algorithms are part of the much bigger software made for analysis of the data provided by a SEM. If access to the software was acquired, it was tried on two samples. The first one is the surface of a tin sphere, cropped in a way that the edges of the image create an inscribed square on the surface of the sphere (Figures 4.1). The second is a ridge in an indium wire (Figures 4.2).
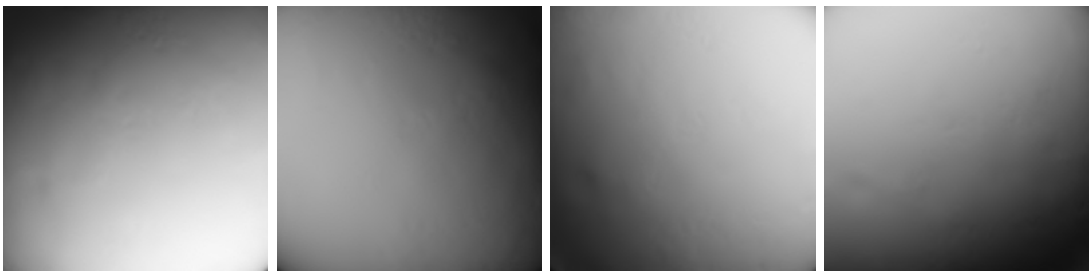
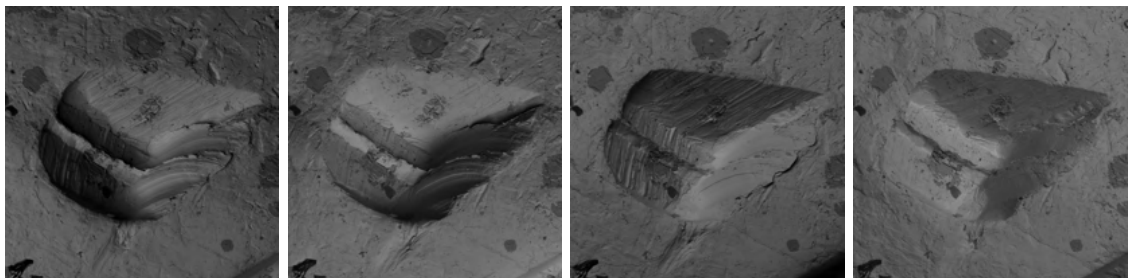Figure 4.1: Surface of the sphere acquired with 4-segment BSE detector.

Figure 4.2: A ridge in an indium wire acquired with 4-segment BSE detector.

It should be noted that the author is by no means an expert in operating of the software mentioned in this chapter. All of the software were input the same sample images, and the best result achieved is presented. Because the presented software is complicated in nature, it is possible that some advanced settings could improve the achieved results.

4.1   DigitalSurf - Mountains

DigitalSurf's software has been around since 1990. The Mountains software has a wide range of supported instruments, such as profilometers, AFMs, SEMs, and more. Their algorithm works with four segments of the detectors as with couples of two opposite segments, where each couple specialises on east-west or south-north slopes. They claim that the Mountains software can work with a 4-segment detector and even with a 3-segment BSE detector [17]. The calculation is very quick (less than a second).

The software requires calibration to achieve quantitative results. The calibration standards must be supplied by the instrument manufacturer. Because no calibration standards were available at the time of writing this work, the calibration could not be performed.

Examples

The software trial version is publicly available, and the company even kindly provided a monthly extension of the license. It was tested on the samples without prior calibration, and no data had to be input manually. The software suggested even the correct spatial configuration of images. An attempt to calibrate the software for the sample has been made; however, the results after calibration were not presentable, probably because of some misunderstanding of configuration parameters.
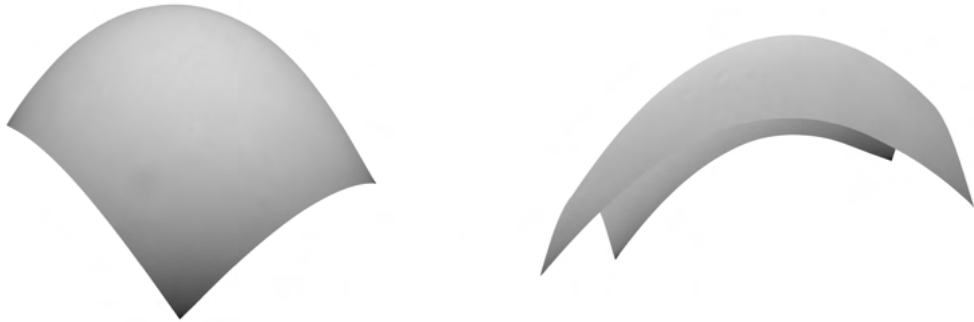
Figure 4.3: Reconstucted surface of a tin sphere using DigitalSurf Mountains.

In Figure 4.3, it can be seen that one side of the model is much lower than the other side. This is probably caused by improper relative calibration of the detector segments, resulting in different brightness and contrast of acquired images. The 3D model has been vertically scaled in order to highlight the spherical nature of the surface. That is to be expected, as the software was not calibrated.

The surface of the sample 4.2 is quite wavy with no distinct curvature. The curvature is to be expected, as the surface of the imaged wire was round.
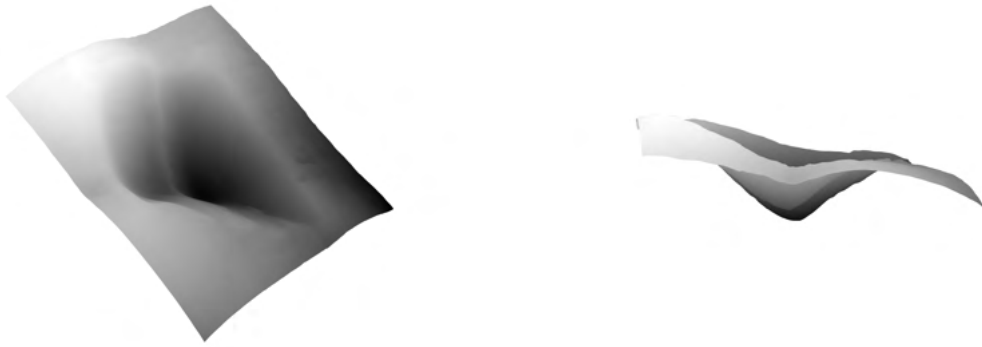
Figure 4.4: 3D model of a ridge in an indium wire reconstucted by DigitalSurf Mountains.

4.2 Point Electronic M2C - microShape

Point electronic GmbH is a German company based in Halle (Saale). They provide the electronics and software for SEM and TEM. Moreover, the company provides a full-fledged solution tailored specifically for the topography reconstruction, including scanning hardware, acquisition software, analysis software, and calibration standards. The software microShape is able to reconstruct the topography of the sample using the 4-segment BSE detector, as well as visualise and evaluate the 3D model [12].

The company was kind enough to provide a trial version of the software, which was tried out, and a few results can be found below. It must be mentioned that in order to obtain quantitative 3D measurements, the system must be calibrated. Because the acquisition system was not calibrated for the software, only qualitative measurements are possible.

Examples

The trials were done with no prior calibration of the software. A few parameters must have been input manually because the metadata of the image did not contain them. The parameters were the working distance, the radial distance between the detector centres and the optical axis and WD correction (distance between the detector and the last lens level). There was a possibility to input offset calibration for each image, which was not used.

Figure 4.5: Reconstucted surface of a tin sphere using Point Electronic microShape.

Both models are pictured immediately after the reconstruction, with no post-modifications. The precision of reconstruction of uncalibrated samples was impressive, to say the least.

Figure 4.6: 3D model of a ridge in an indium wire reconstucted by Point Electronic microShape.

The calculations took about a second for each model. Figure 4.5 shows that the software managed to capture the approximately true shape of the surface without deformations caused by improper calibration of the detector segments. The software even managed to capture the curvature of the surface in Figure 4.6.

4.3   Hitachi map 3D

A well-known manufacturer of various technology, Hitachi, provides software for 3D reconstruction. An attempt to acquire a trial version of the software has been made; however, it was unsuccessful. All of the provided information is obtained from their website [4].

No reconstruction speed claims have been found. Regarding measurement performance, in the specification of the software is written: „*Measurement performance varies depending on calibration accuracy, the condition of the type of specimen, the observation mode, and the observation condition.*" What calibration is required has not been specified. The detectable range is claimed to be $\pm60°$ [4].

Chapter 5

Proposed solution

This chapter will sum up the current situation and emphasise the space for improvement. Furthermore, a solution implemented in this work will be presented, tools used in this work, basic assumptions and the main focus of the work will be described.

5.1 Analysis of the current situation

The photometric stereo with reflectance maps proposed by Woodham [37] has been around for a long time. Most of the current implementations are focused on the photometric stereo with light. Because of the different reflectance properties of the electrons, this method must be adapted. Moreover, obtaining quantitative measurement instead of qualitative is a challenge by itself because of many variables influencing the resulting radiation. To the author's knowledge, there are few such solutions that are able to provide qualitative measurement.

Solutions described in Chapter 4 work well even with not calibrated systems, even though no quantitative measurement can be guaranteed. The software relies on the calibration samples provided with the system or external.

One of the goals of this work is to design the system pre-calibrated using estimated reflectance maps that will keep the reflectance characteristics of the material. These reflectance maps can be then modified according to the current microscope setup. The second goal is to implement the photometric stereo algorithm calibrated on tin samples that is able to estimate the 3D surface model of SEM samples with reasonable precision using reflectance maps.

5.2 Assessment

Photometric stereo from images acquired from BSE detectors is not a trivial task, as the characteristics of BSE emittance are heavily dependent on the whole measuring setup. In order to simplify the study, a few assumptions had to be made. The assumptions have been made after consultation with both the supervisor and the TESCAN consultant.

- **The sample is made out of tin** - To remove dependency on the material from the resulting solution, tin samples were chosen. This is because of the difficult quantification of reflectance characteristics of materials with different atomic numbers. It has been proven that the atomic number influences the angular distribution of the

backscattered electrons (See 2.3). Still, no exact measurements or formulas have been found at the time of writing this thesis.

- **Detector gain and offset are constant** - Quantification of detector settings to the shades of grey has proven to be a challenging task with unreliable results. While the basic principle of the gain and offset can be easily represented as a mathematical operation (Eq. 2.4), the coefficients are not easily acquired. Even though acquisition software does provide a number describing the gain and offset, they are dimensionless numbers that represent the internal settings of the microscope in a given environment. For example, a different temperature of the detector changes the meaning of the number, effectively preventing reliable conversion to a number meaningful to levels of grey in the acquired image. The solution for this problem in this work is to make the variable a constant, meaning that algorithms will be calibrated for single values of the gain and offset.

Considering these assumptions, the remaining variables affecting the calculations are:

- The energy of the incident beam

- The electron beam current

- The working distance

These variables had to be taken into account when designing the algorithm. Its basis stands on the estimation of reflectance maps according to the current environment. The goals set for this work had been to create a system of reasonable speed that can reliably reconstruct the topography of the specimen for which it was calibrated. If the sample does not satisfy the calibration conditions, for example, it is made out of a different material, a reasonable estimate of the topography should be produced. The proposed steps of the algorithm are as follows:

1. **Estimation of the reflectance maps** - The reflectance maps should be created to approximate reflectance maps matching the current setup. All variables mentioned previously must be taken into account.

2. **Calculation of the map of normal vectors** - After the reflectance maps are created, the algorithm will use them to estimate surface normal at every point of the image.

3. **3D reconstruction** - Use the map of normal vectors to estimate surface topography. The simplest method that comes to mind is integrating the map of normal vectors. However, this approach does not consider cumulative error, which is more prominent the further away from origin integration takes place. An appropriate method of minimalising the cumulative error must be used to reach a satisfactory result.

5.3   Implementation tools

Because of the large number of calculations that take place when computing a 3D model, the programming language C++20 has been chosen as the implementation language to take advantage of potential greater execution speeds. However, for rapid prototyping and the creation the auxiliary tools, the usage of the Python programming language was decided.

The OpenCV library was to be used for operations on images, which is available for both C++ and Python. This allowed for an easy transition between the prototype in python to optimised C++ code. For the user interface programming, the author decided to use the Qt 6.2 framework.

5.4 Dataset and ground truth

In order to analyse reflectance characteristics and model them via reflectance maps, a large dataset of the images of tin spheres was to be acquired. Because their surface contains every possible inclination that could be seen by a detector, they are ideal for the task. The dataset contains images acquired at working distances (WD) from 10mm to 20mm, equally spaced 2mm apart. At each working distance, the tin spheres were imaged with different beam energies, ranging from 5keV to 30keV, with the step of 5 keV. The offset and gain of the detector were kept constant, at 56.3% and 33.3%, respectively. If the image turned out to be too bright/dark, the brightness was modified by modifying the beam current (BC).

Because of the known shape of the tin spheres, the height information is available implicitly. Because of this, the dataset can be used to assess the precision of the algorithm without additional measurements with other techniques/tools.
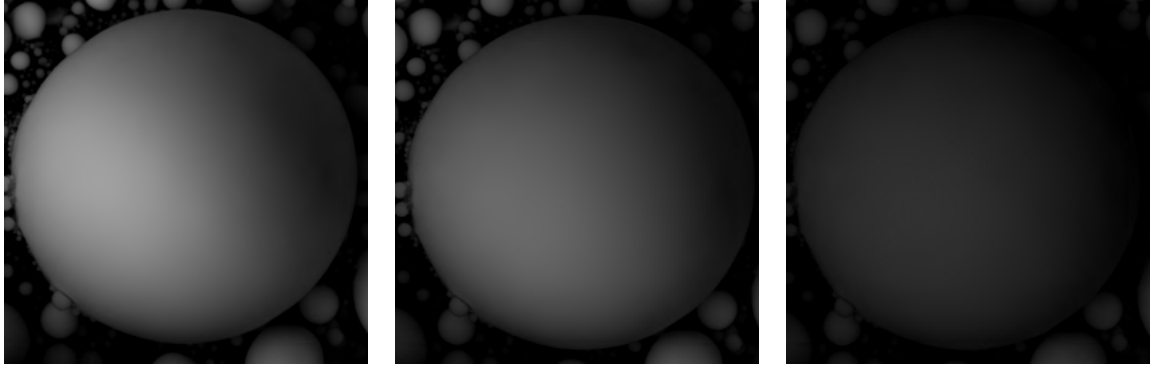
Dataset examples

The following are the tin spheres from the calibration dataset. The images are representatives of the various acquisition parameters to show the various dependencies.
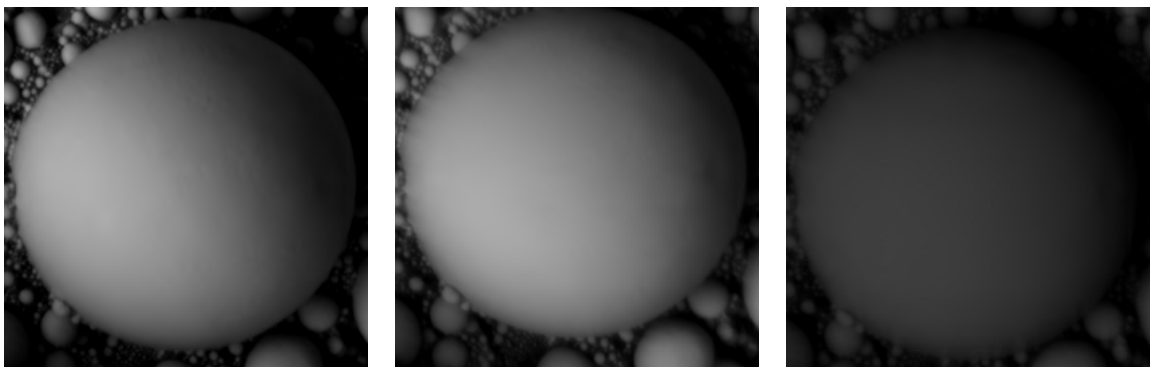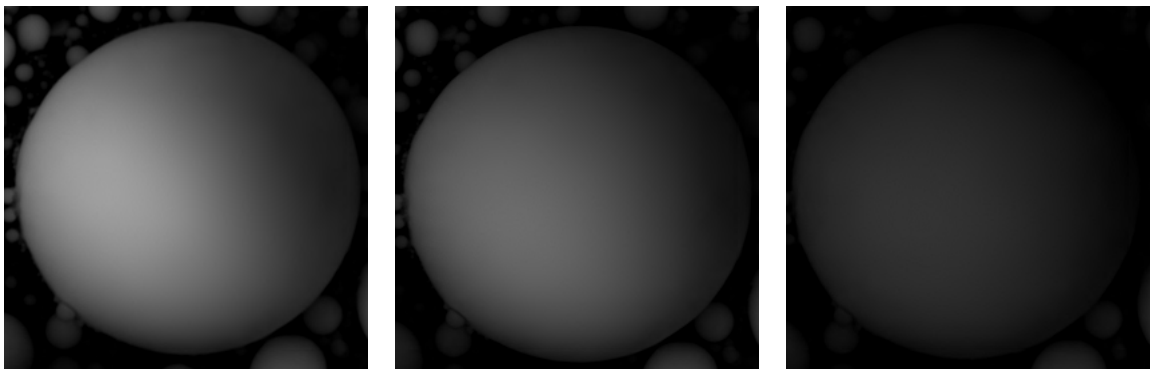

(a) BC = 7nA, WD = 10mm   (b) BC = 10nA, WD = 14mm   (c) BC = 10nA, WD = 20mm

Figure 5.1: Tin spheres acquired with landing energy of 5keV.

(a) BC = 1.1nA, WD = 10mm   (b) BC = 1.1nA, WD = 14mm   (c) BC = 1.3nA, WD = 20mm

Figure 5.2: Tin spheres acquired with landing energy of 20keV.

(a) BC = 750pA, WD = 10mm   (b) BC = 750pA, WD = 14mm   (c) BC = 900pA, WD = 20mm

Figure 5.3: Tin spheres acquired with landing energy of 30keV.

Chapter 6

Implementation

This chapter describes the inner workings of the algorithm in detail. The algorithm itself consists of three steps, with one additional that must be done before the execution of the program in order to obtain the best results. The schema of the algorithm is as shown in Figure 6.1.
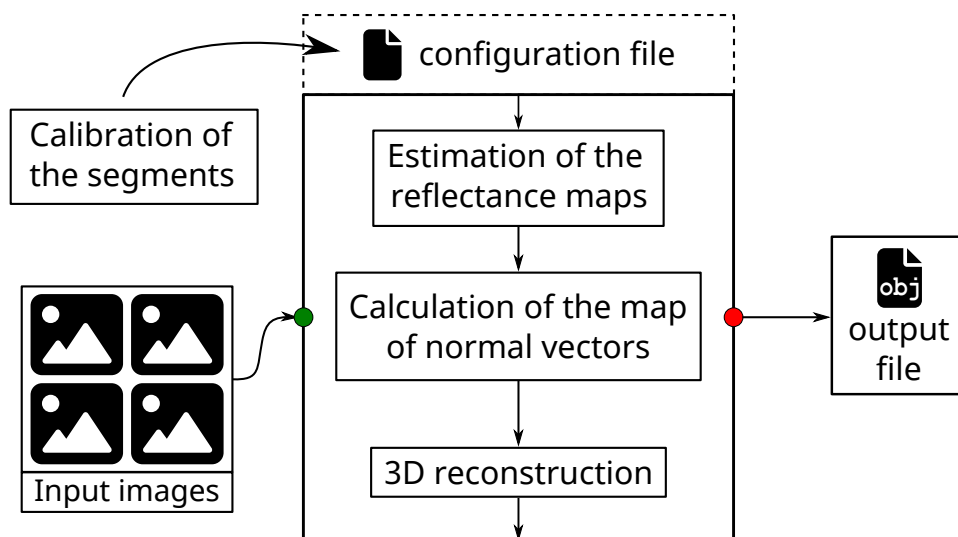
Figure 6.1: Block diagram of the algorithm.

Description of the individual blocks from Figure 6.1.

- **Calibration of the segments** - prior to any reconstruction, detector segments must be calibrated relative to each other

- **Modifications of the images** - after the images have been input to the algorithm, they are modified by the coefficients saved in the configuration file with calibration results

- **Estimation of the reflectance maps** - internal settings of the microscope are loaded from the image metadata, and reflectance maps are estimated

- **Calculation of the map of normal vectors** - a map of normal vectors is obtained using previously estimated reflectance maps

- **3D reconstruction** - surface topography is reconstructed from the map of the normal vectors

6.1 Calibration of the detector segments

If all detector segments measure the same intensity for the same relative surface inclination, only one reflectance map has to be created. This created reflectance map can be adapted for each detector segment by rotating it by multiple of 90°. For this to be possible, segments have to be calibrated relative to each other. This is, however, not the case for every microscope and most certainly not for one where the tin spheres dataset was acquired (Figure 6.2). For this reason, the software contains detector settings, where it is possible to set calibration coefficients. The coefficients are the same as the gain and offset equation coefficients (Equation 2.4). Each segment has its own set of these coefficients.
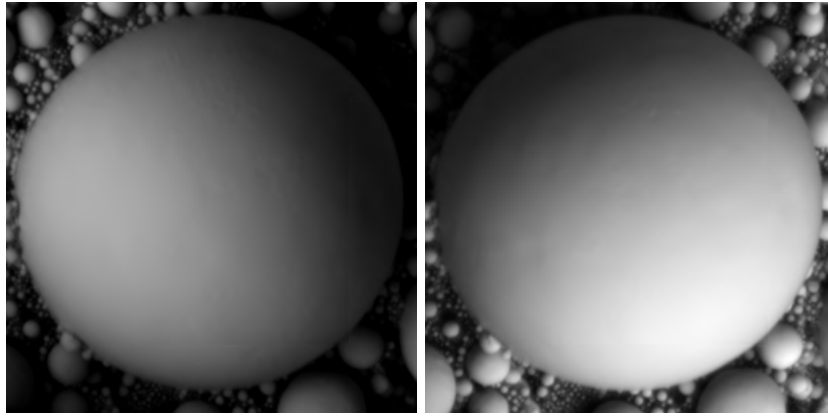

Figure 6.2: The image acquired at the same time at 5keV, 10mm WD, 7 nA BC with the same gain and offset settings but from different detector segments. The image on the right is brighter than the image in the left.

A tool was created to help with finding the fitting coefficients. It attempts to match the histograms by finding two points of interest and aligning them. The first point of interest is the global maximum, and the second is the last non-zero value. It is effective only for the images where the amount of shades is expected to be equal from all directions, e.g., a sphere. For the best results, it is recommended to erase the background of the calibration sample. The tool can be found in the repository under ./Tools/autocalibration.py.

The testing of various images acquired under different conditions from the dataset concluded that the calibration coefficients between segments remain approximately constant. Thus, it is sufficient to execute this step of the algorithm just once, provided that the detector configuration does not change.

In the detector settings is one additional parameter, the port angle. Sometimes, the plane of rasterisation is not aligned with the axes of the detector, which causes a shift in the measured surface inclination (Figure 6.4). The setting of this parameter compensates for this shift. The images in Figure 6.2 would require compensation of approximately 60°.
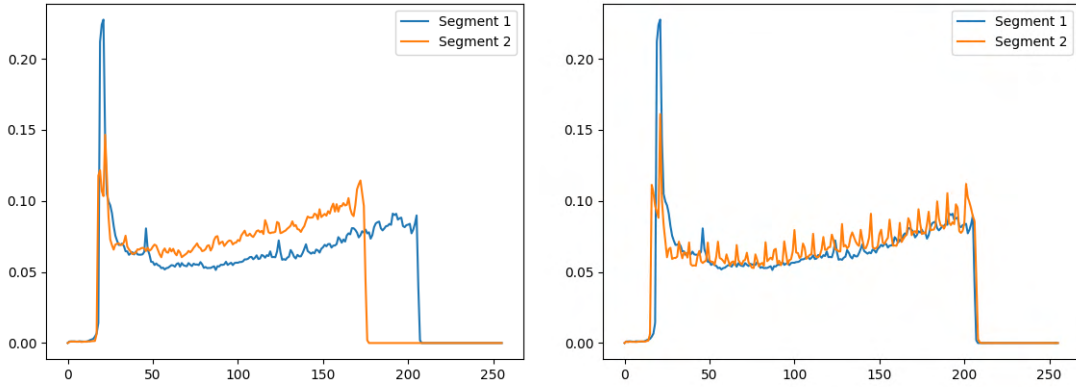
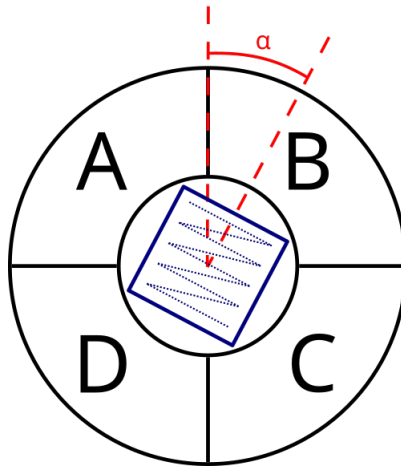Figure 6.3: Histograms of the images before modification (left) and after (right).

Figure 6.4: Topdown schema of the BSE detector (black) and scanning plane (blue). The scanning plane is rotated by the angle α, for which the algorithm must be calibrated.

6.2   Estimation of the reflectance maps

The reflectance maps as proposed by [37] are defined in the gradient space, which is not ideal for computers, as it approaches the positive and negative infinity in the extremums. To solve this problem, a new type of reflectance map is proposed. The map is defined in the „spherical" space. The easiest way to imagine it is that the reflectance map is the topdown view of the perfect sphere as seen by a detector segment in given conditions. The calculation of the surface inclination is very straightforward. Assume that the origin of the coordinate system is directly in the middle of the map that ranges from (-1,1) on both axes. The surface unit normal vector can be calculated as [x,y,z], where x and y are coordinates on the map, and z is calculated as Eq. 6.1.

$$z = \sqrt{1 - x^2 - y^2} \tag{6.1}$$

This representation is ideal, as the reflectance maps characteristics are inferred from the tin spheres. However, the closer the normal is to the extremums, the sparser the information about the surface inclination gets. In other words, a single step of some size near the centre corresponds to a smaller angular shift than the same step near the edge of
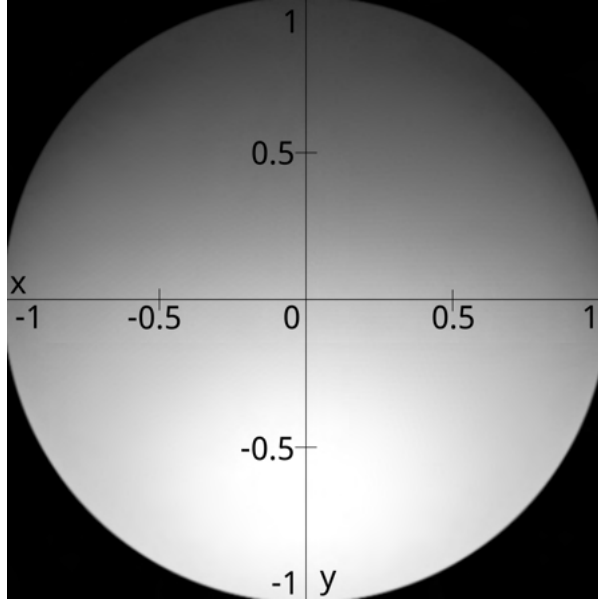
Figure 6.5: An example of the reflectance map in the spherical space.

the map. This tradeoff is manageable, as the data acquired from the dataset suffer from the same deficiency.

The normal map in this form could be processed and created as a bitmap. Nevertheless, later operations of estimating the surface inclination would require thousands of lookup operations in these bitmaps that could be sped up by precalculating the data needed; however, the processing complexity would still be an issue. Moreover, a method for the creation of arbitrary big bitmaps would need to be created in order not to limit the precision of the estimated reflectance map.

An estimation method using Principal Component Analysis (PCA) was considered. The idea was to sample the dataset with an equally spaced set of n points that would create an n-dimensional vector for each dataset image. The set of vectors would then be analysed using PCA, creating a set of basis vectors. These vectors could be used to approximate all of the reflectance maps with an arbitrary precision that would be guaranteed by the choice of basis vectors.

The second approach considered was an approximation of the reflectance characteristics using some mathematical function. When filtering values from the reflectance maps, an ellipsoidal shape emerges, as seen in Figure 6.6.

Because of the ellipsoidal nature of the resulting shapes, the approximating function could be defined by a few parameters, and the calculation of the shape intersections could be solved analytically.

After careful consideration of both approaches, the latter was chosen. The approximating curve was chosen to be the Lamé curve, also known as the superellipse. In the Cartesian coordinate system, it is analytically defined as

$$\left| \frac{x+h}{a} \right|^c + \left| \frac{y+k+b}{b} \right|^c = 1 \tag{6.2}$$

where a is a half-width of the superellipse, b is half-height, h is the shift on the x-axis, k is the shift on the y-axis, and c is the „coefficient of angularity". The greater c is,
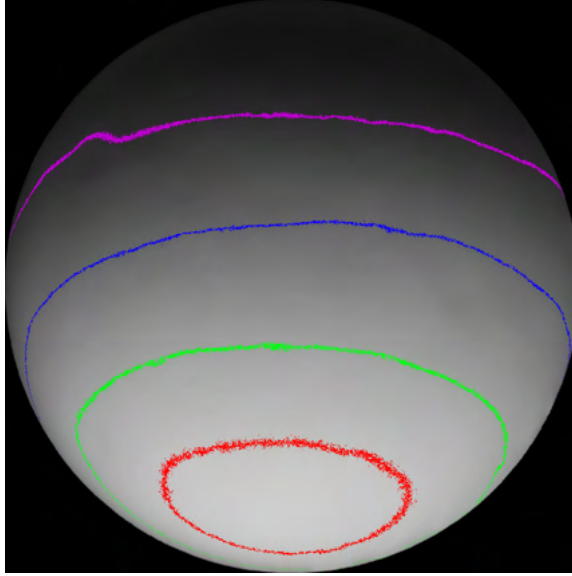
Figure 6.6: The acquired image from the dataset with specific pixel values highlighted. Because the image is a real-life example, the resulting shapes are not perfect. However they are sufficient to approximate reflectance characteristics. Color-values: Red-192, Green-161, Blue-101, Purple-43

the more rectangle-like is the superellipse. If c equals 2, the curve represents an ordinary ellipse. The equation 6.2 was designed to expand towards negative numbers with the top of the superellipse stationary. It is because of the automatic superellipse fitting algorithm described later. An example of the superellipse representing the isoline can be seen in Figure 6.7

Thus, every reflectance map can be represented by a set of 256 superellipses, where five parameters define each superellipse. A correct swapping of the parameters can realise the rotation of the reflectance maps for each detector segment, so the Equation 6.2 does not need to account for any rotation.

Superellipse fitting

The dataset had to be processed to find out the parameters of superellipses that describe reflectance maps. Because at this point, the segments should be calibrated relative to each other, only images from the reference segment needed to be processed. To maximise fitting accuracy, every image of a tin sphere acquired with a given segment was modified. The modifications consist of stretching the sphere to fill as much of the image as possible without cropping the sphere and painting the remaining background black. Care was taken to ensure that the symmetry axis was aligned with the coordinate y-axis. Modified images were then processed by an algorithm specifically designed for this purpose.

The algorithm uses a hill-climbing optimisation technique to ensure the best fit of the superellipse. For each image, it runs 255 iterations. Each iteration at first masks out pixels with the intensity from range <1,255> and then fits the superellipse for the masked out pixels. The mask is thinned to contain a curve with a 1px width to avoid prioritising optimisation towards the wider lines. The algorithm fits only for parameters a, b, c, and k. The h parameter does not need to be fitted, as a horizontal shift should not occur. The
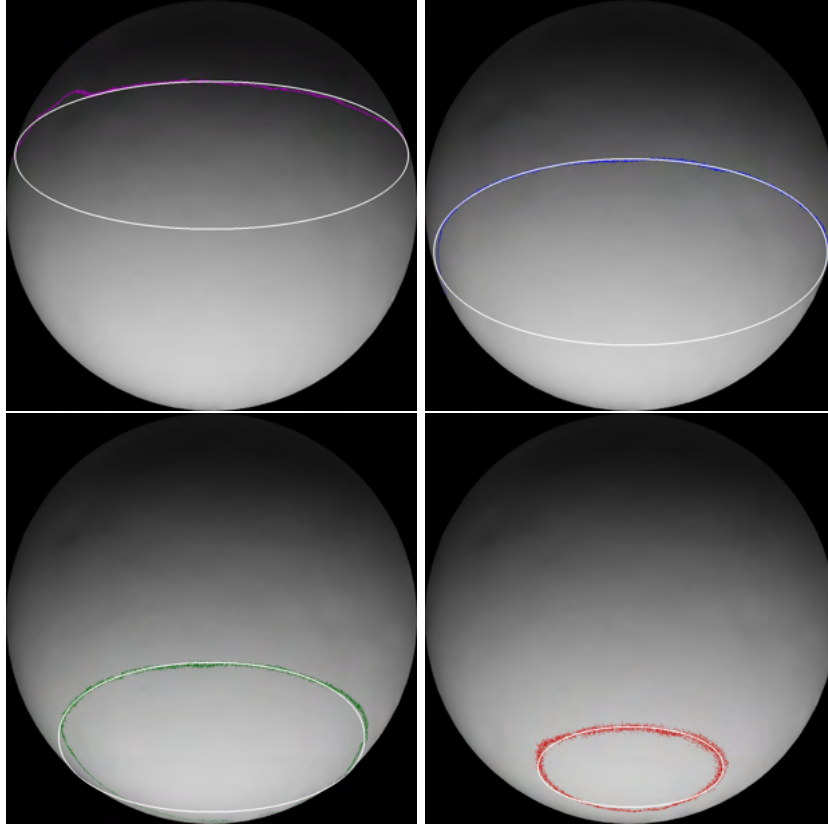
Figure 6.7: Image with various pixels filtered, overlayed with a superellipse.

algorithm contains a setting for the automatic rotation of the image to compensate for the image illumination could be rotated because of the angle between the scanning plane and detector axis (Figure 6.4). Because the hill-climbing algorithm finds only a local maximum, a reasonable starting guess should be provided.

A few heuristics were used here. First, the algorithm expects the specular point to be on the lower half of the sphere. The specular point is the point with maximum pixel intensity. It is reasonable to expect the whole superellipse or only the upper part of it to be visible if this is true (similarly to Figure 6.6). The value of the k parameter will then be approximately the y coordinate of the topmost masked out pixel. The a parameter is set to be half of the difference between the rightmost and leftmost pixel. Finally, the b parameter was set to be half of the a parameter for the lack of a better estimation. In the end, all of the superellipse parameters were normalised using the width or height (a by the width, b and k by the height) of the original images to find out relative parameters.

The optimisation constraint was chosen to be a least-squares approach. The sum of squares was calculated as squares of euclidean distances between a masked out pixel and the closest point on the estimated superellipse.

The tool created for automatic ellipse fitting can be found in ./Tools/ellipseTools/vectorize.py. Example of the fitting result provided in Figure 6.8.
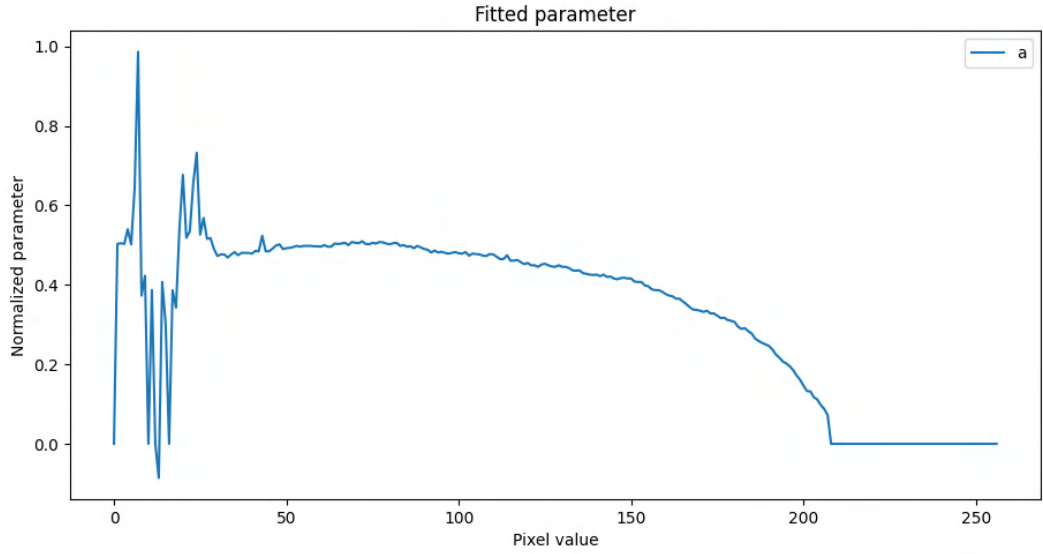
Figure 6.8: Graph of the fitted parameter a of the superellipse for the sphere acquired at 5keV, 10mm and 7nA.

Interpolation of the superellipse parameters

At this point, the superellipses are parametrised. However, because it is inconvenient to keep direct parameters due to difficult interpolation of the secondary relations, the results of the automatic fitting were interpolated using the Piecewise Cubic Hermite Interpolating Polynomial (PCHIP) with a set of 33 points. Because fitting was run on all of the possible pixel values and the image does not contain pixels with values in full range, some results are meaningless. Thus, the PCHIP interpolates only a meaningful part of the fitting parameters. The boundaries of the meaningful part are important, too, as secondary relations can be deduced from them. The result of such interpolation is then a set of 15 points and two numbers representing the meaningful range. This has to be done manually, as it is difficult to find the meaningful range and filter out noise automatically. A tool was made for this task that can be found in ./Tools/spline_builder.py (an example of the tool can be seen in Figure 6.9).

After all of the parameters are interpolated with the PCHIP, the next step is to interpolate the points of the PCHIPs. This allows for finding relations between the images and generating reflectance maps dependence on the electron beam current, energy and working distance. For an in-depth explanation, please refer to the appendix A.

6.3   Calculation of the map of normal vectors

The algorithm used in this part of the program is the same as described in Section 3.4, but reflectance maps are used in the form as described in Section 6.2. The steps for the estimation of the surface normal in a point are as follows.

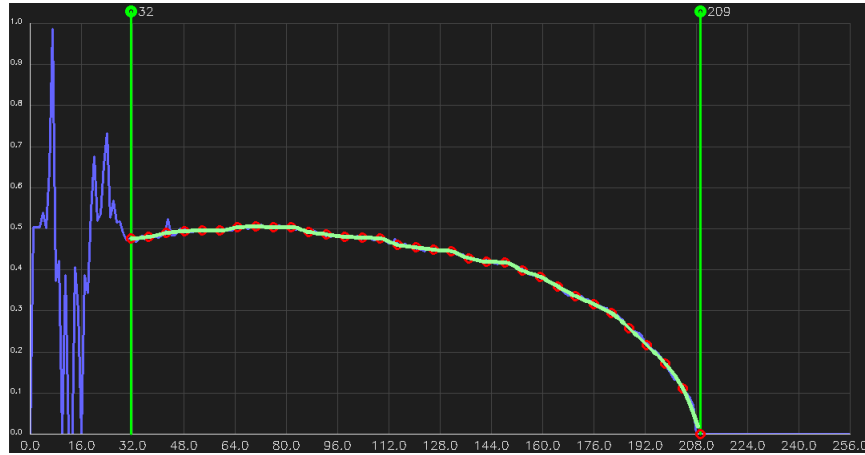1. A pixel from each image is selected. The position of the pixel must be the same relative to the image.

Figure 6.9: Graph of the interpolation PCHIP (green) overlaying fitted parameter a. Green vertical lines are boundaries of the meaningful range.

2. For each of the four selected pixels, a superellipse is estimated based on the intensity and microscope settings at the time of the acquisition.

3. Points of interest are calculated for each superellipse pair. Points of interest are either intersections of superellipses or, in the case of no intersection, the closest two points of the superellipses.

4. A single point of interest is selected from each superellipse pair in a way that the resulting cluster of selected points is as close to one another as possible.

5. The average of selected points of interest is considered to be the surface normal in a point.

These steps are iterated over every pixel of the image, resulting in a map of the normal vectors.
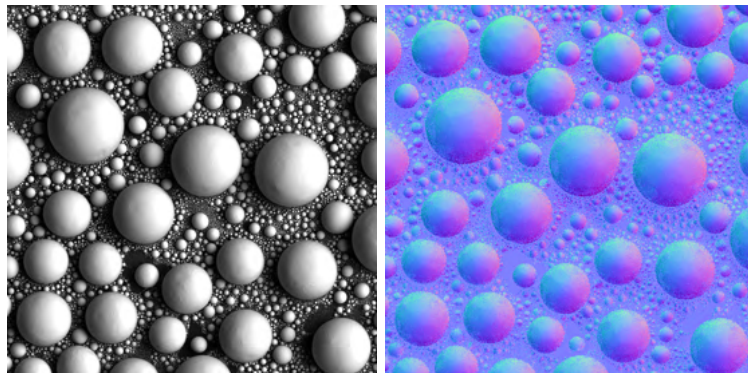
Figure 6.10: Result of the calculation of normal vectors. On the left is one of the images from which the normal map was calculated. On the right is the map of the surface normals, where normals are encoded in the colours of the image.

35

Optimisations

Because the computation of the intersections is most likely to be repeated multiple times for the same superellipses, it makes sense to precalculate the intersections beforehand. After precalculation, the step of finding points of interest can be degraded to lookup in a convenient structure.

The precalculation of the superellipses interactions does not influence the calculation of other intersections. This makes it ideal for multithreading acceleration, as no synchronisation must be done between threads.

6.4   3D reconstruction

The most straightforward approach to 3D reconstruction of the surface from the map of normal vectors is the integration of the map. The surface normals can be transformed into the derivatives of the surface. However, because of the noise in the normal map, this method is heavily influenced by the cumulative error. The further from the origin the integration takes, the more significant the error is. This results in surface discontinuities and deformations.

Several methods have been employed to minimise the integration error [27] [33] [1]. Most often, a method uses a least-squares approach. In this work, a method as described in the literature [38] is used. The author was kind enough to provide an implementation, which is used in this work.

In the beginning, a quadrangular facet for each of the normals is created. The next phase of the algorithm is iterative and consists of two significant steps called local shaping and global blending. In local shaping, each facet is projected onto a plane defined by normal in the point. Global blending attempts to modify a mesh surface in a way that satisfies the positions of vertices in all of the facets and is not discontinuous. The error of such deformation is calculated by means of least squares. In this work, the algorithm was modified to allow for greater deformation of facets with normals of greater inclination. This modification was done because tests have shown that measurement accuracy of normal angle drops with greater inclinations.
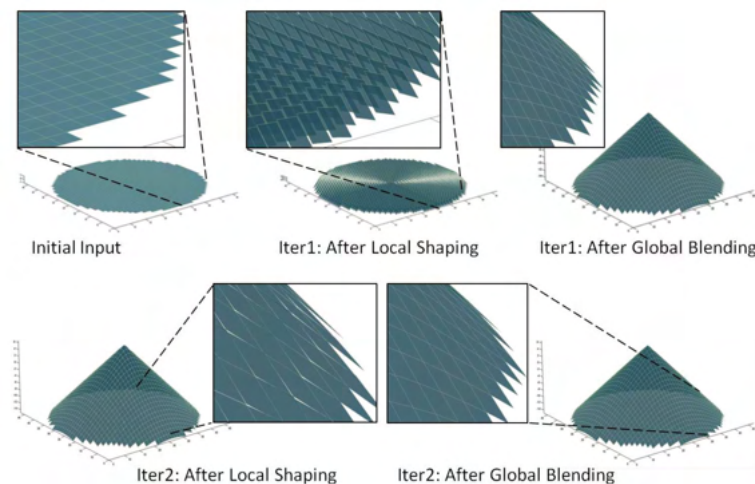

Figure 6.11: Visualisation of local shaping and global blending. [38]

The provided implementation of the algorithm does not handle big images well. For this reason, the software automatically downscales bigger images to the resolution of 512*512.

Chapter 7

Evaluation and testing

The evaluation chapter can be split into three sections. In the first section, the accuracy of the reconstructed 3D model is considered. The second section is examples of the samples without known topography but with material characteristics similar to the tin. The third section shows samples that are not in the calibration range of the algorithm.

7.1 Known topography/suitable material characteristics

To evaluate the accuracy of the reconstructed 3D model, a reference model must be known. However, the only available samples with known topography for this thesis are tin spheres. For this reason, the tin spheres are reused as follows. A square cut is taken from the original image in such a way that the edges of the cut image create an inscribed square on the surface of the sphere. The resulting image is with a minimal noise introduced by the background, shadows, and normal vectors approaching 90° inclination. A few sets of images were modified in this way, each set acquired under different conditions. For each 3D model, a diagonal cross-section compared to the perfect circle is shown.

It can be seen that none of the 3D models are perfect, but the overall shape fits the circle pretty well. Imperfections are to be expected, as the samples were acquired in real-life and are subject to various noises. The edges of the cross-sections in Figures 7.3, 7.6, 7.9 do not span the full half-circle, as one could expect. This error is introduced by the difficult measurement of surface normals close to the extremums. Moreover, the edges of the images are the most prone to the effects of aberrations caused by the imperfect settings of the microscope. The model 7.8 is visibly more flat than other models. This is caused by the poor estimation of the reflectance maps.
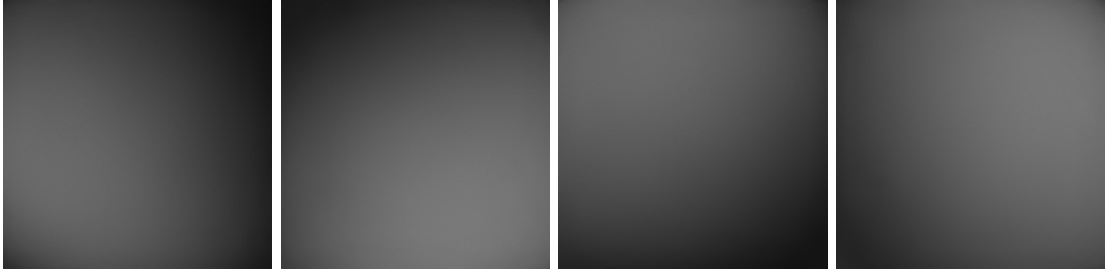
Figure 7.1: Sample of the tin spheres acquired at 20 keV, 14mm and 1,1nA.

Figure 7.2: Reconstructed model of the surface of the tin sphere acquired at 20 keV, 14mm and 1,1nA.
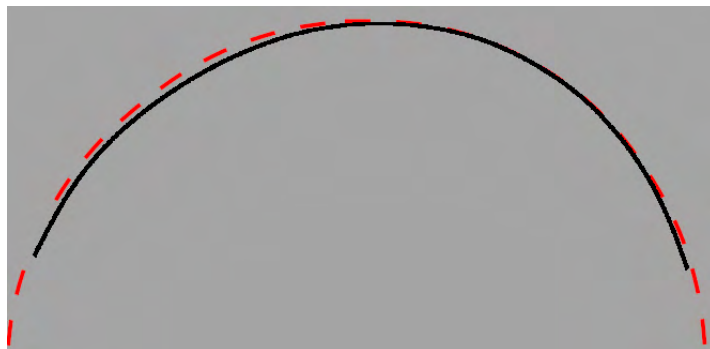

Figure 7.3: Diagonal cross section of the reconstructed model (black) compared to the perfect circle(red).
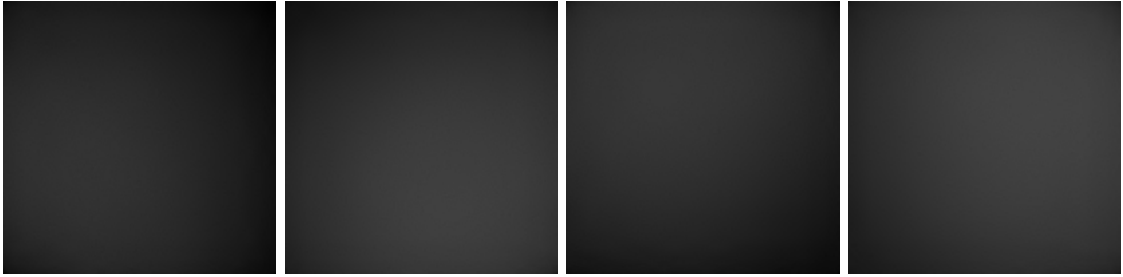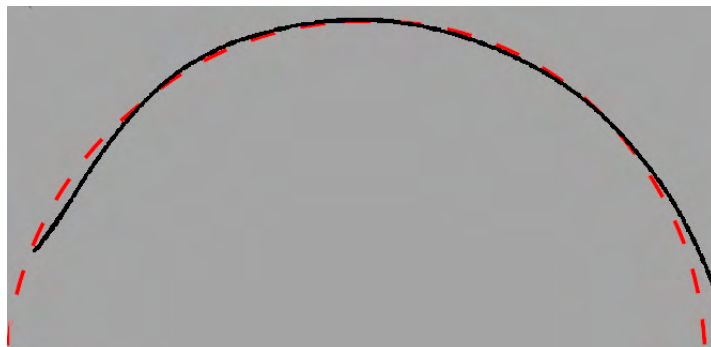
Figure 7.4: Sample of the tin spheres acquired at 30 keV, 20mm and 0,9nA.

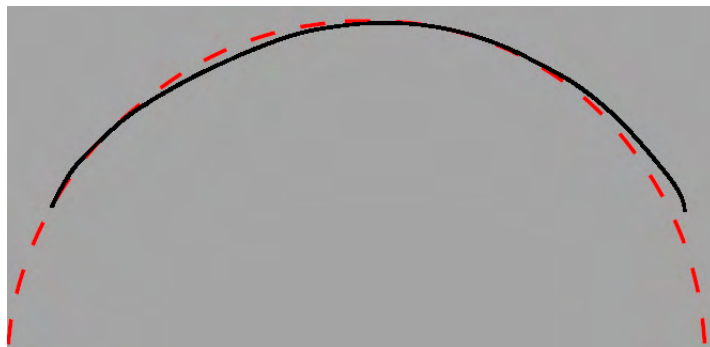Figure 7.5: Reconstructed model of the surface of the tin sphere acquired at 30 keV, 20mm and 0,9nA.

Figure 7.6: Diagonal cross section of the reconstructed model (black) compared to the perfect circle(red).

Figure 7.7: Sample of the tin spheres acquired at 5 keV, 12mm and 10nA.

Figure 7.8: Reconstructed model of the surface of the tin sphere acquired at 5 keV, 12mm and 10nA.

Figure 7.9: Diagonal cross section of the reconstructed model (black) compared to the perfect circle(red).

7.2 Unknown topography/suitable material characteristics

Here are a few examples of the reconstruction of the non-spherical samples. The accuracy of the reconstruction cannot be evaluated, as the real topography is not known. The examples are to demonstrate the abilities of the algorithm on the different samples.
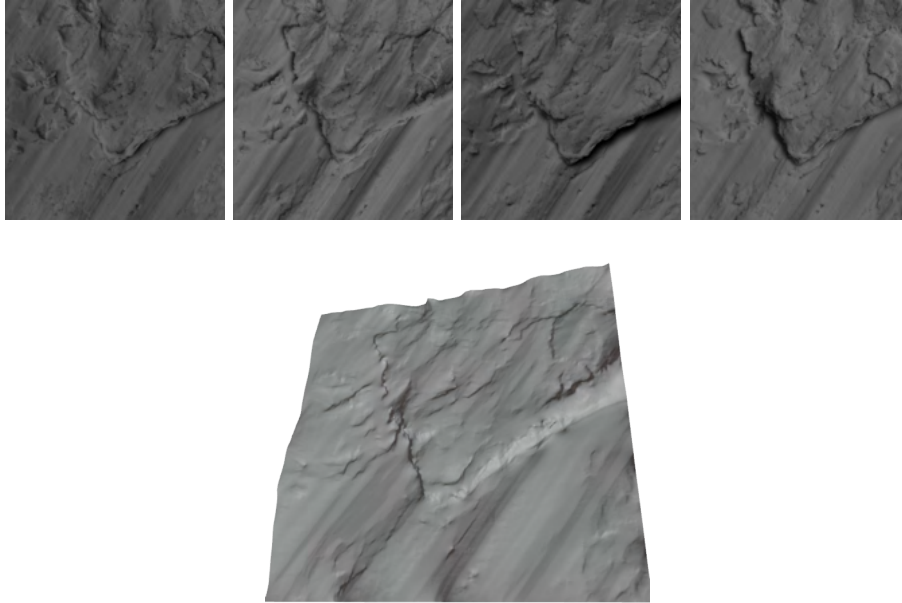

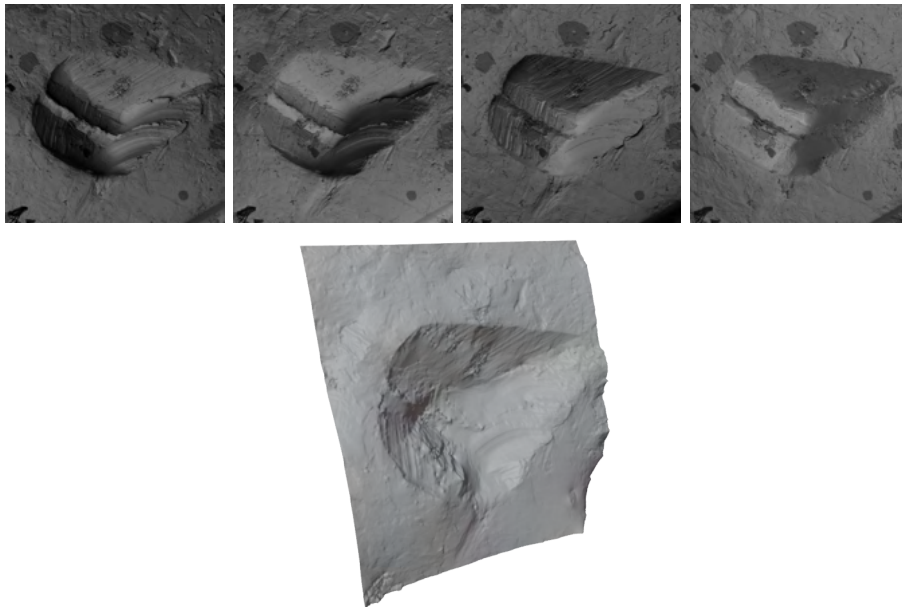Figure 7.10: 3D model of the cliff-like feature on the surface of the bulk tin.

Figure 7.11: 3D model of the ridge on the surface of the indium wire.

It can be seen that even without known topography, 3D models show features one would expect. The indium in Figure 7.11 was used because its atomic number is very similar to
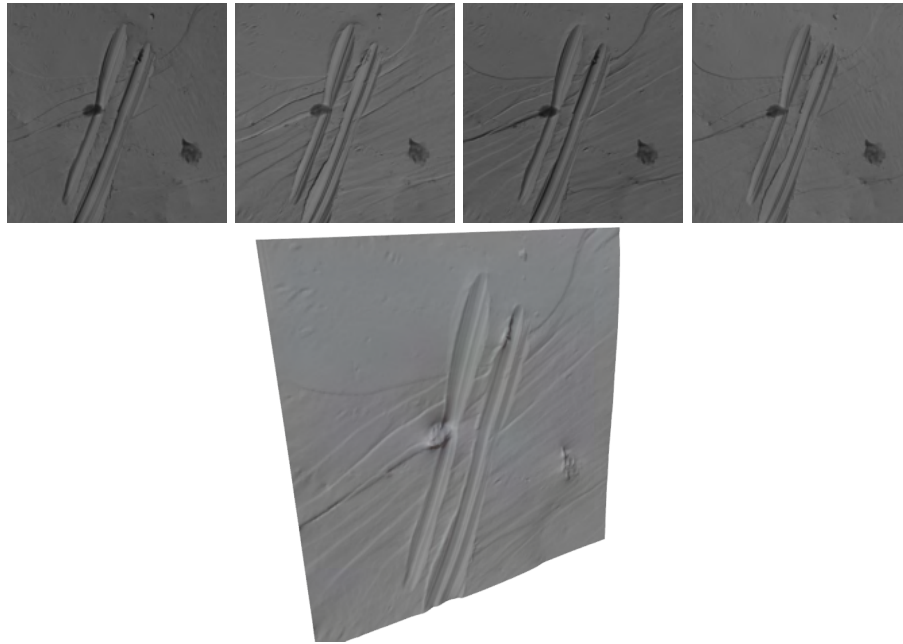
Figure 7.12: 3D model of the scratch in the bulk tin.

the atomic number of tin, so the assumption was made that reflectance characteristics are very similar to the characteristics of the tin.

7.3 Unknown topography and material

The algorithm can be used to reconstruct the topography of the samples with different material characteristics as for which it was calibrated. However, the resulting 3D model can be used at most for qualitative measurement. When no reasonable assumption can be made to estimate correct reflectance maps, the algorithm can be set to use one general map that is able to process most of the images with reasonable brightness and contrast.
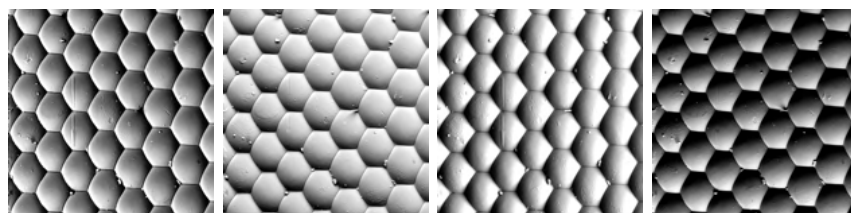

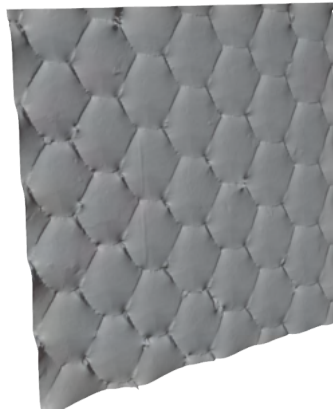Figure 7.13: BSE images of the eye of the fly.

Figure 7.14: 3D model of the eye of the fly, reconstructed with the estimated parameters.

Figure 7.15: 3D model of the eye of the fly, reconstructed with the general parameters.

When reconstructed with estimated parameters, Figure 7.14, the 3D features are very indistinct. When parameters for the estimation of the general reflectance map were used, the resulting model is rich in spatial features (Figure 7.15).

Chapter 8

Conclusion

The goal of this work was to implement the photometric stereo algorithm calibrated on tin samples that is able to estimate the 3D surface model of SEM samples with reasonable precision using reflectance maps. The goal has been fulfilled.

The literature regarding the backscattered electrons' properties and their detectors has been studied. The result was a list of detector parameters and physical properties which had to be accounted for. The photometric stereo algorithms have been studied as well, and the system exploiting differences in measured local intensities has been proposed. The procedure for calibration of the system has been developed and carried out. External implementation of the reconstruction algorithm for the reconstruction of the 3D model from the map of normal vectors has been successfully used.

The resulting software is able to reconstruct the samples that fall into its calibration range with good precision. It is able to reconstruct the samples for which it was not calibrated, although the resulting model is just qualitative. The whole pipeline is of reasonable speed; the maximum reconstruction time achieved was about 30 seconds.

This work has been an exciting endeavour. It accompanied much learning in a foreign field; however, the process was quite enjoyable.

Future work includes removing the constraints set in this work, e.g. constant offset and gain, single material. This would require refining the calibration procedure, as the proposed one is quite laborious. A change in microscope configuration, such as replacing the BSE detector with another model with different geometry, would require complete recalibration of the system. If the reflectance characteristics, for example, the angular distribution of backscattering, would have been quantified, a physics-based model would be a viable option.

In the future, an iterative algorithm could be developed that attempts to minimise error calculated in the 3D reconstruction step. That could be achieved by tweaking the parameters which have been obtained by the reflectance map estimator. Maybe even autocalibration would be possible. The estimator itself needs more work, as the current guessing of the reflectance maps parameters is „blind". The algorithm could be improved by a verification if all the measured intensities fall into the estimated range and modify it accordingly.

The calculation of the normal map always tries to find the intersections of the whole superellipses. However, for the approximation of the isolines, sometimes just part of the superellipse is needed. Removing this unneeded information could lead to faster and more precise calculations of normal vectors.

Bibliography

[1] AGRAWAL, A., CHELLAPPA, R. and RASKAR, R. An algebraic approach to surface reconstruction from gradient fields. In: *Tenth IEEE International Conference on Computer Vision (ICCV'05) Volume 1*. USA: IEEE Computer Society, 2005, vol. 1, p. 174–181 Vol. 1. DOI: 10.1109/ICCV.2005.31. ISBN 076952334X01.

[2] APPEN, A. von and BECK, M. Structure Determination of the Nuclear Pore Complex with Three-Dimensional Cryo electron Microscopy. *Journal of Molecular Biology.* 1st ed. European Molecular Biology Laboratory, Structural and Computational Biology Unit, Cell Biology and Biophysics Unit, Meyerhofstraße 1, 69117 Heidelberg, Germany: Journal of Molecular Biology. 2016, vol. 428, no. 10, p. 2001–2010. DOI: 10.1016/j.jmb.2016.01.004. ISSN 00222836. Available at: https://linkinghub.elsevier.com/retrieve/pii/S0022283616000231.

[3] BOEHME, L., BRESIN, M., BOTMAN, A., RANNEY, J. and HASTINGS, J. T. Focused electron beam induced etching of copper in sulfuric acid solutions. *Nanotechnology.* 1st ed. Department of Electrical and Computer Engineering, University of Kentucky: IOP Publishing Ltd. 2015-12-11, vol. 26, no. 49. DOI: 10.1088/0957-4484/26/49/495301. ISSN 0957-4484. Available at: https://iopscience.iop.org/article/10.1088/0957-4484/26/49/495301.

[4] CORPORATION, H. H.-T. 3D Visualization Software Hitachi map 3D. *Analytical Systems, Electron Microscopes & Medical Systems* [online]. [cit. 03-05-2022]. Available at: https://www.hitachi-hightech.com/global/science/products/microscopes/electron-microscope/tabletop-microscopes/map3d/#top. Path: TOP > Products & Services > Electron Microscopes / Atomic Force Microscopes > Electron Microscopes (SEM/TEM/STEM) > Tabletop Microscopes > 3D visualization software Hitachi map 3D.

[5] DOMINIQUE DROUIN, B. I. s. monte CArlo SImulation of electroN trajectory in sOlids. *Casino* [online]. [cit. 03-05-2022]. Available at: https://www.gegi.usherbrooke.ca/casino/index.html.

[6] EATON, P. and WEST, P. *Atomic Force Microscopy.* Requimte, and Faculty of Science, University of Porto: OUP Oxford, 2010. ISBN 9780191576676. Available at: https://books.google.sk/books?id=R_9QEAAAQBAJ.

[7] EGERTON, R. F. *Physical principles of electron microscopy : an introduction to TEM, SEM, and AEM.* New York: Springer, 2008. ISBN 978-0-387-25800-3.

[8] ERNI, R., ROSSELL, M. D., KISIELOWSKI, C. and DAHMEN, U. Atomic-Resolution Imaging with a Sub-50-pm Electron Probe. *Physical Review Letters.* 1st ed. National

Center for Electron Microscopy, Lawrence Berkeley National Laboratory, Berkeley, California 94720, USA: APS Physics. 2009, vol. 102, no. 9. DOI: 10.1103/PhysRevLett.102.096101. ISSN 0031-9007. Available at: https://link.aps.org/doi/10.1103/PhysRevLett.102.096101.

[9] EULITZ, M. and REISS, G. 3D reconstruction of SEM images by use of optical photogrammetry software. *Journal of Structural Biology*. 1st ed. Institute for Anatomy and Clinical Morphology, School of Medicine, Faculty of Health, Witten/Herdecke University, Alfred-Herrhausen-Straße 50, D-58448 Witten, Germany: Elsevier. 2015, vol. 191, no. 2, p. 190–196. DOI: 10.1016/j.jsb.2015.06.010. ISSN 10478477. Available at: https://linkinghub.elsevier.com/retrieve/pii/S1047847715300149.

[10] FOSTER, S. and HALBSTEIN, D. *Integrating 3D Modeling, Photogrammetry and Design*. 1st ed.th ed. London: Springer London, 2014. ISBN 978-1-4471-6328-2.

[11] F.R.S., L. R. XII. On the manufacture and theory of diffraction-gratings. *The London, Edinburgh, and Dublin Philosophical Magazine and Journal of Science*. 1st ed. London: Taylor & Francis. 1874, vol. 47, no. 310, p. 81–93. DOI: 10.1080/14786447408640996. Available at: https://doi.org/10.1080/14786447408640996.

[12] GMBH point electronic. *SEM topography* [online]. Point electronic GmbH [cit. 2022-05-10]. Available at: https://www.pointelectronic.de/en/products/topography/.

[13] GOLDSTEIN, J. I., JOY, D. C., MICHAEL, J. R., NEWBURY, D. E., RITCHIE, N. W. et al. *Scanning Electron Microscopy and X-Ray Microanalysis*. 4th ed. 2018th ed. Imprint: Springer„ 2018. ISBN 9781493966769.

[14] HAWKES, P. W. and SPENCE, J. C. H. *Springer Handbook of Microscopy*. 1st ed.th ed. Cham: Springer International Publishing, 2019-11-2. ISBN 978-3-030-00068-4. Available at: https://link.springer.com/book/10.1007/978-3-030-00069-1.

[15] LTD., J. *A Guide to Scanning Microscope Observation* [online]. 1st ed. JEOL Ltd. [cit. 2022-05-10]. Available at: https://www.jeol.co.jp/en/applications/pdf/sm/844_en.pdf.

[16] LTD., J. *Scanning Electron Microscope A To Z* [online]. 1st ed. JEOL Ltd. [cit. 2022-05-10]. Available at: https://www.jeol.co.jp/en/applications/pdf/sm/sem_atoz_all.pdf.

[17] MIGNOT, C. *Using a four-quadrant detector: how to give your SEM images a 3D upgrade* [online]. Digital Surf [cit. 2022-05-10]. Available at: https://www.digitalsurf.com/blog/using-a-four-quadrant-detector-in-3d-reconstruction/.

[18] OLIENSIS, J. Uniqueness in shape from shading. *International Journal of Computer Vision*. 1st ed. Computer and Information Science, University of Massachusetts at Amherst, 01003, Amherst, MA: Springer. 2004, vol. 6, p. 75–104. DOI: https://doi.org/10.1007/BF00128151. ISSN 1573-1405. Available at: https://link.springer.com/article/10.1007/BF00128151.

[19] ORLOFF, J. *Handbook of Charged Particle Optics*. CRC Press, 2017. ISBN 9781420045550. Available at: https://books.google.cz/books?id=y0FF19lud5YC.

[20] PHOTOGRAMMETRY, A. S. for and SENSING, R. Definitions. *What is ASPRS?* [online]. [cit. 03-05-2022]. Available at: https://www.asprs.org/organization/what-is-asprs.html. Path: Home -> Society Info -> What is ASPRS?

[21] POSTEK, M. T., KEERY, W. J. and FREDERICK, N. V. Low-profile high-efficiency microchannel-plate detector system for scanning electron microscopy applications. *Review of Scientific Instruments*. 1st ed. Microelectronics Dimensional Metrology Group, National Institute for Standards and Technology, Technology Building A-347, Gaithersburg, Maryland 20899: AIP Publishing. 1990, vol. 61, no. 6, p. 1648–1657. DOI: 10.1063/1.1141127. ISSN 0034-6748. Available at: http://aip.scitation.org/doi/10.1063/1.1141127.

[22] PRADOS, E. and FAUGERAS, O. Shape From Shading. In: PARAGIOS, N., CHEN, Y. and FAUGERAS, O., ed. *Handbook of Mathematical Models in Computer Vision* [online]. 1st ed. Boston, MA: Springer US, 2006, p. 375–388. DOI: 10.1007/0-387-28831-7_23. ISBN 978-0-387-28831-4. Available at: https://doi.org/10.1007/0-387-28831-7_23.

[23] PUTTEN, E. G. van, AKBULUT, D., BERTOLOTTI, J., VOS, W. L., LAGENDIJK, A. et al. Scattering Lens Resolves Sub-100 nm Structures with Visible Light. *Phys. Rev. Lett.* [online]. 1st ed. USA: American Physical Society. May 2011, vol. 106, p. 193905, [cit. 2022-03-03]. Physical Review Letters. DOI: 10.1103/PhysRevLett.106.193905. ISSN 1079-7114. Available at: https://link.aps.org/doi/10.1103/PhysRevLett.106.193905.

[24] REIMER, L. *Scanning Electron Microscopy*. 2ndth ed. Berlin, Heidelberg: Springer Berlin Heidelberg, 1998. ISBN 978-3-642-08372-3.

[25] SAINI, M., SINGH, R., SOORAJ, K. P., BASU, T., ROY, A. et al. Cold cathode electron emission with ultralow turn-on fields from Au-nanoparticle-decorated self-organized Si nanofacets. *Journal of Materials Chemistry C*. 1st ed. Odisha, India: Royal society of chemistry. 2020-12-17, vol. 8, no. 47, p. 16880–16895. DOI: 10.1039/D0TC03862H. ISSN 2050-7526. Available at: http://xlink.rsc.org/?DOI=D0TC03862H.

[26] SANTO, H., SAMEJIMA, M. and MATSUSHITA, Y. Numerical shape-from-shading revisited. *IPSJ Transactions on Computer Vision and Applications*. 1st ed. Graduate School of Information Science and Technology, Osaka University, Osaka, Japan: [b.n.]. 2018, vol. 10, no. 1. DOI: 10.1186/s41074-018-0044-9. ISSN 1882-6695. Available at: https://link.springer.com/10.1186/s41074-018-0044-9.

[27] SMITH, G. and BORS, A. Height estimation from vector fields of surface normals. In: [online]. 1st ed. Santorini, Greece: [b.n.], July 2002, vol. 2, p. 1031 – 1034 vol.2. DOI: 10.1109/ICDSP.2002.1028266. ISBN 0-7803-7503-3. Available at: https://www.researchgate.net/publication/3964099_Height_estimation_from_vector_fields_of_surface_normals.

[28] TSIKOURAS, B., PE PIPER, G., PIPER, D. J. and SCHAFFER, M. Varietal heavy mineral analysis of sediment provenance, Lower Cretaceous Scotian Basin, eastern

Canada. *Sedimentary Geology.* 1st ed. Patras, Greece: Elsevier. 2011, vol. 237, 3-4, p. 150–165. DOI: 10.1016/j.sedgeo.2011.02.011. ISSN 00370738. Available at: https://linkinghub.elsevier.com/retrieve/pii/S0037073811000650.

[29] UKRAINTSEV, V. Review of reference metrology for nanotechnology: significance, challenges, and solutions. *Journal of Micro/Nanolithography, MEMS, and MOEMS.* 1st ed. Nanometrology International, Inc. Allen, Texas: Journal of Micro/Nanolithography, MEMS, and MOEMS. 2012-01-01, vol. 11, no. 1. DOI: 10.1117/1.JMM.11.1.011010. ISSN 1932-5150. Available at: http://nanolithography.spiedigitallibrary.org/article.aspx?doi= 10.1117/1.JMM.11.1.011010.

[30] VENTURI, F. *New approaches for phase manipulation and characterisation in the transmission electron microscope.* Via Università 4, 41121 Modena, 2018. Dissertation. UNIVERSIT 'A DEGLI STUDI DI MODENA E REGGIO EMILIA.

[31] VERNON PARRY, K. Scanning electron microscopy: an introduction. *III-Vs Review.* 1st ed. Centre for Electronic Materials, UMIST, France: Elsevier. 2000, vol. 13, no. 4, p. 40–44. DOI: 10.1016/S0961-1290(00)80006-X. ISSN 09611290. Available at: https://linkinghub.elsevier.com/retrieve/pii/S096112900080006X.

[32] VOLKERT, C. A. and MINOR, A. M. Focused Ion Beam Microscopy and Micromachining. *MRS Bulletin.* 1st ed. Cambridge University Press. 2007, vol. 32, no. 5, p. 389–399. DOI: 10.1557/mrs2007.62. ISSN 1938-1425. Available at: https://link.springer.com/article/10.1557/mrs2007.62.

[33] WANG, M., XIE, W. and CUI, M. Surface Reconstruction with Unconnected Normal Maps: An Efficient Mesh-Based Approach. In: *Proceedings of the 28th ACM International Conference on Multimedia.* New York, NY, USA: Association for Computing Machinery, 2020, p. 2617–2625. ISBN 9781450379885. Available at: https://doi.org/10.1145/3394171.3413920.

[34] WILLIAMS, D. B. *Transmission electron microscopy : a textbook for materials science.* Second editionth ed. New York: Springer, 2009. 5 p. ISBN 978-0-387-76500-6.

[35] WINSTON, P. H. and HORN, B. *The psychology of computer vision.* 1stth ed. Massachusetts Institute of Technology, Artificial Intelligence Laboratory, 545 Technology Square, Cambridge, MA 02139, U.S.A.: McGraw-Hill, 1975. ISBN 0070710481 9780070710481.

[36] WOLF, P., DEWITT, B. and WILKINSON, B. *Elements of Photogrammetry with Application in GIS, Fourth Edition.* 4thth ed. New York: McGraw-Hill Education, 2013. ISBN 9780071761116.

[37] WOODHAM, R. J. Photometric Method For Determining Surface Orientation From Multiple Images. *Optical Engineering.* 1st ed. University of British Columbia (Canada): [b.n.]. 1980-02-01, vol. 19, no. 1. DOI: 10.1117/12.7972479. ISSN 0091-3286. Available at: http: //opticalengineering.spiedigitallibrary.org/article.aspx?doi=10.1117/12.7972479.

[38] XIE, W., ZHANG, Y., WANG, C. C. and CHUNG, R. C.-K. Surface-from-Gradients: An Approach Based on Discrete Geometry Processing. In: *2014 IEEE Conference on*

Computer Vision and Pattern Recognition. 1st ed. Chinese university of Hong Kong: [b.n.], 2014, p. 2203–2210. DOI: 10.1109/CVPR.2014.282. ISBN 978-1-4799-5118-5.

[39] Xu, C. S., Hayworth, K. J., Lu, Z., Grob, P., Hassan, A. M. et al. Enhanced FIB-SEM systems for large-volume 3D imaging. *ELife.* 1st ed. Janelia Research Campus, Howard Hughes Medical Institute, United States; Dalhousie University, Canada; University of California, United States; Lawrence Berkeley National Laboratory, United States; University of North Carolina, United States: eLife Sciences Publications, Ltd. may 2017, vol. 6, p. e25916. DOI: 10.7554/eLife.25916. ISSN 2050-084X. Available at: https://doi.org/10.7554/eLife.25916.

[40] Zhang, Y., Payne, D. N. R., Kong, C., Khan, M. U., Fung, T. H. et al. Advanced Characterisation of Black Silicon Surface Topography with 3D PFIB-SEM. In: *2019 IEEE 46th Photovoltaic Specialists Conference (PVSC)* [online]. 1st ed. UNSW SydneySchool of Photovoltaic and Renewable Energy Engineering: IEEE, 2019, p. 0825–0828. DOI: 10.1109/PVSC40753.2019.8980830. ISBN 978-1-7281-0494-2. Available at: https://ieeexplore.ieee.org/document/8980830/.

Appendix A

In depth description of the interpolation engine

The interpolation engine must be able to estimate the parameters of the superellipse, as described in 6.2. After superellipses were fitted for the dataset images, relations with the beam energy, current, and working distance must have been found. This appendix describes the process of approximating these relations for each superellipse parameter.

For each of the parameters, graphs demonstrating the dependencies on various settings were made. These graphs were then used to determine how the parameter is interpolated. The parameters themselves can be split into two groups. The first one is a group of scalar parameters, where for each processed image, a single number was produced. This group includes the c parameter and boundaries of meaningful data (region of interest). The boundaries can be interpreted as the borders of the histogram values. The second group is array parameters. This includes the a, b and k parameters. These parameters are dependent on the pixel value on top of the microscope settings.

Parameter a

The a parameter is an array parameter. It is surely dependent on the specific pixel value, but other variables are not so clear.

Dependecy on the electron energy

Graphs of the parameter a dependent on the electron energy are shownn in Figure A.1.

It can be seen that there is some dependency, but a subtle one. It is more prominent at greater working distances, where the graphs with bigger energy have flatter curvature. The conclusion is that the parameter a is dependent on the energy of the incident beam.

Dependency on the working distance

The dependency of the parameter a on the working distance can be seen in Figure A.2.

The plotted lines are very similar. Nevertheless, there is no clear dependency on the working distance because the lines are by no means in any order. Thus, the deviations were attributed to the measurement noise.
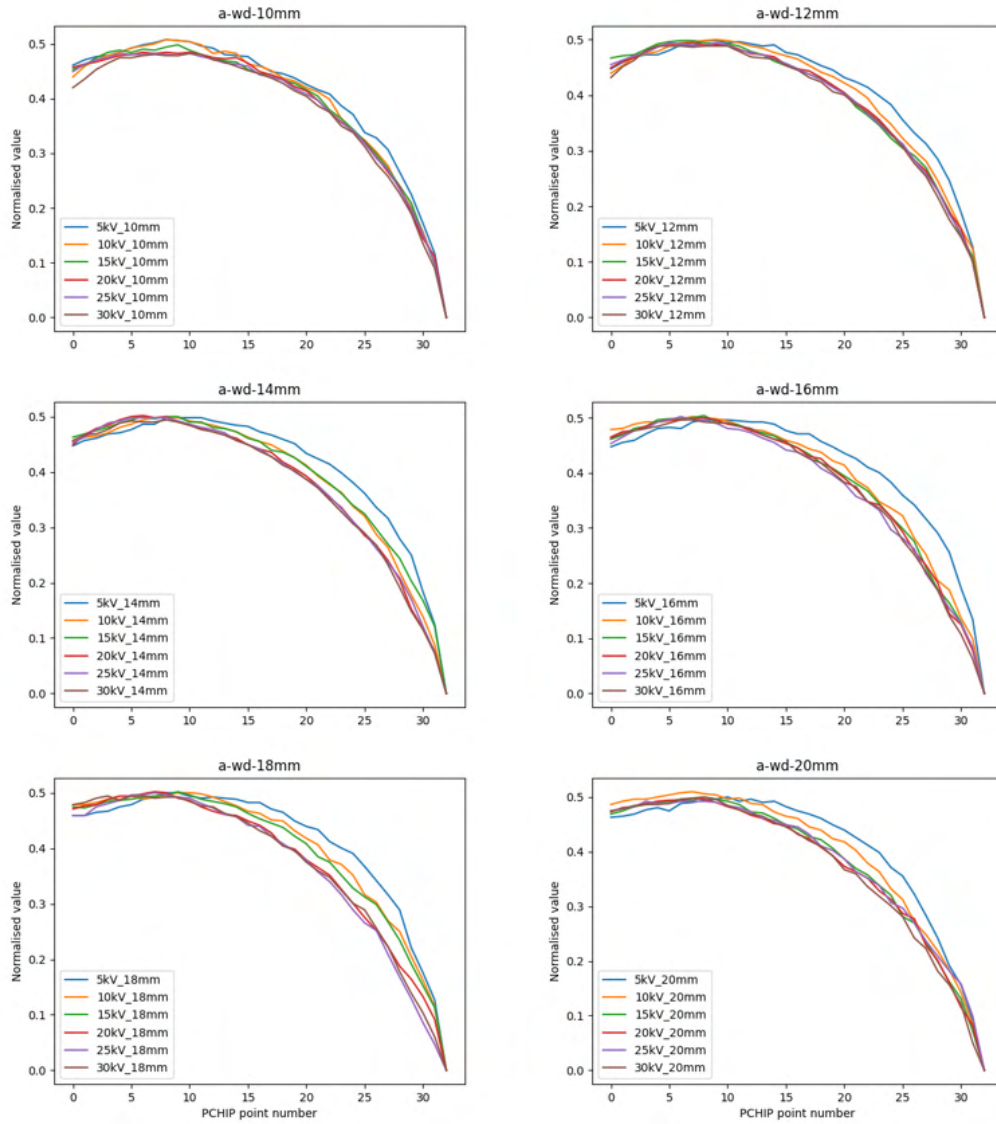
Figure A.1: Graphs of the fitted *a* parameter grouped according to the same working distance.

For the final approximation, only the energy of the electron beam has to be accounted for. Because of this, to minimise the noise, the available data are averaged for the same working distance (Figure A.3). Approximation algorithm is described in section A.
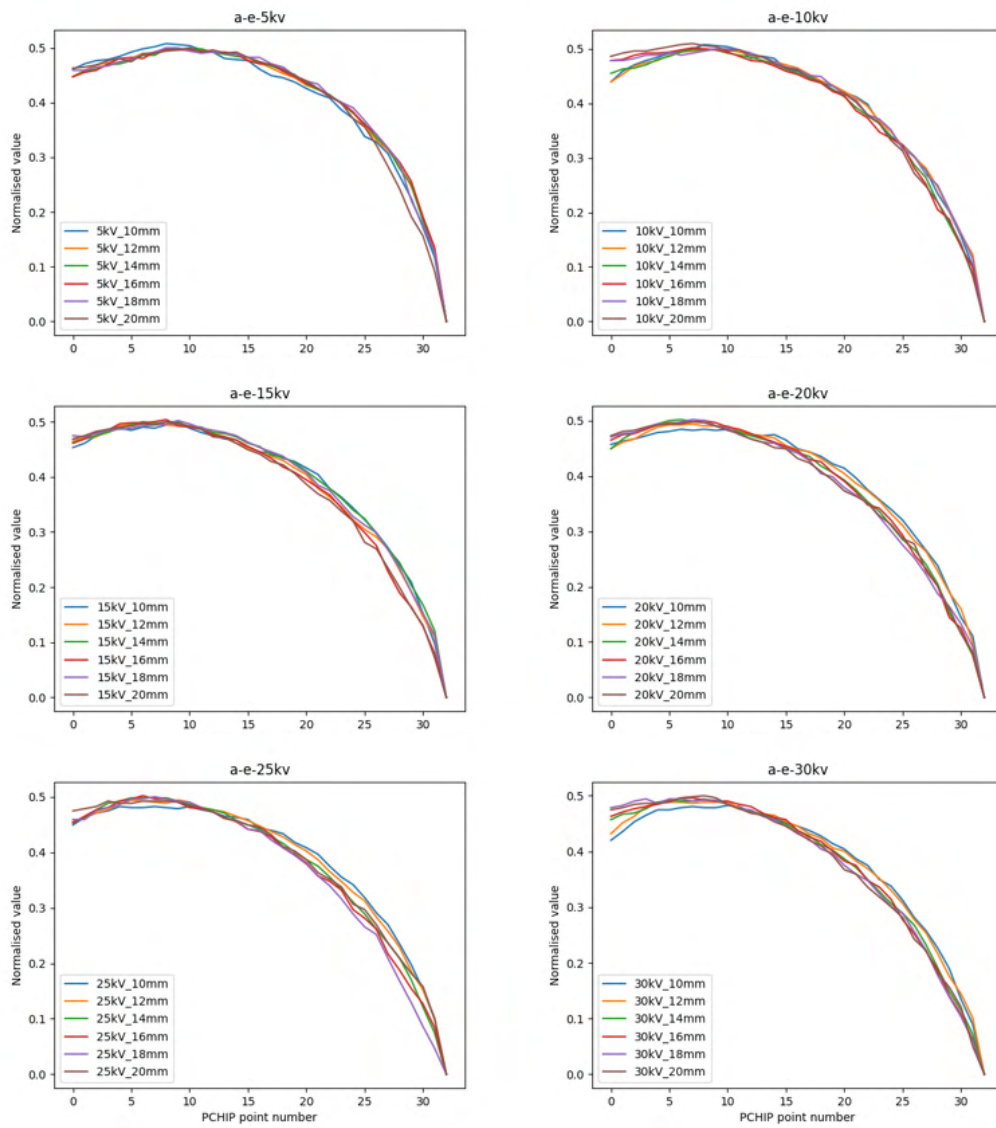
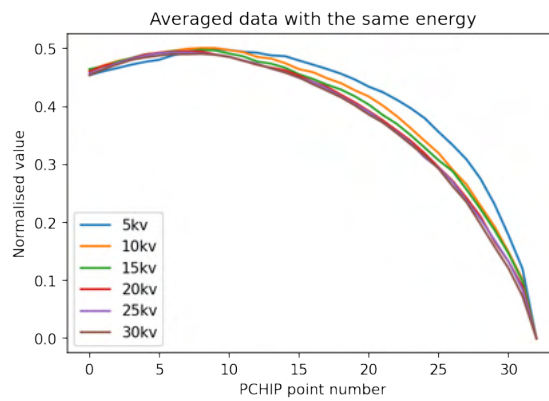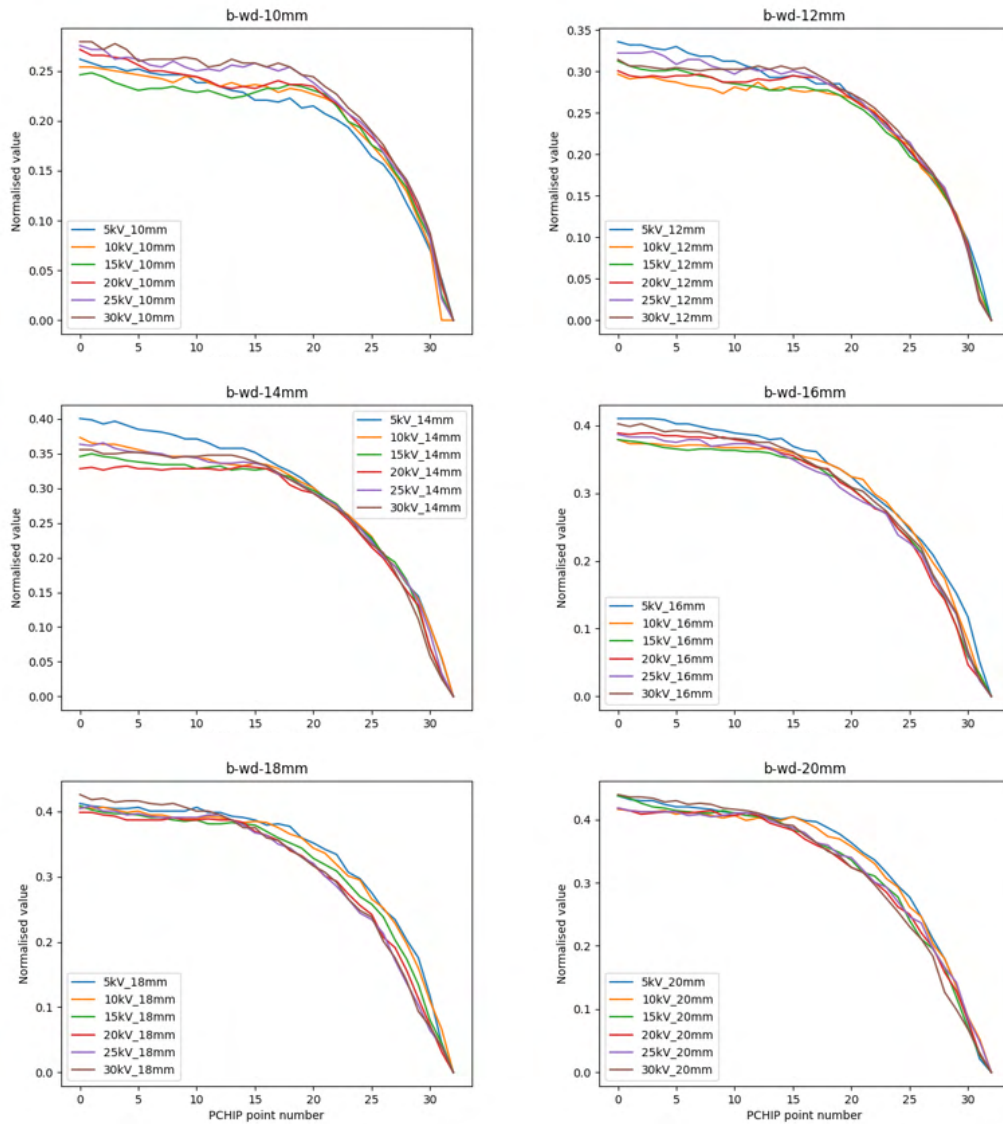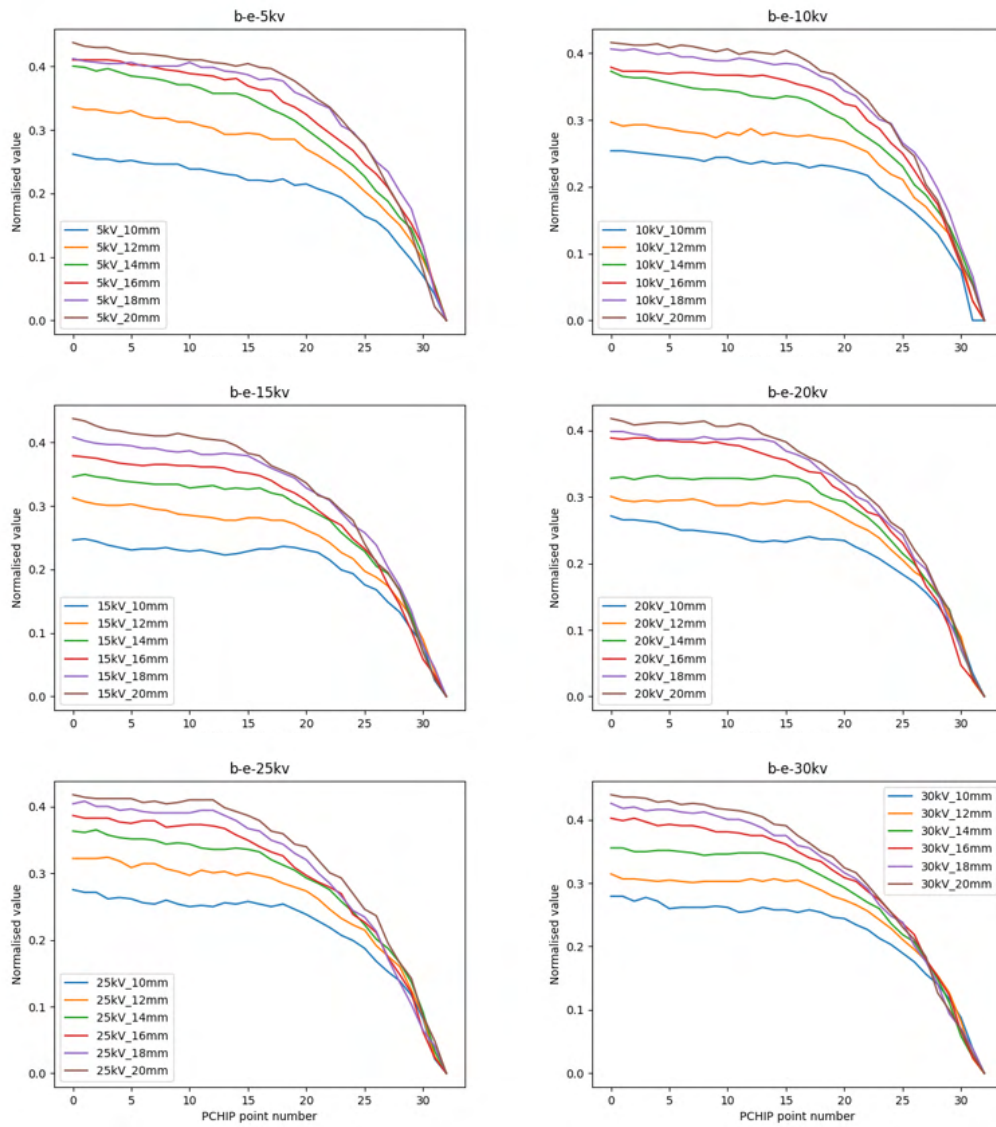Figure A.2: Graphs of the fitted a parameter grouped according to the same energy.

Figure A.3: Averaged data with the same energy.

Parameter *b*

Similarly to the *a* parameter, graphs were made to visualise dependencies on the energy and working distance.

Dependecy on the electron energy

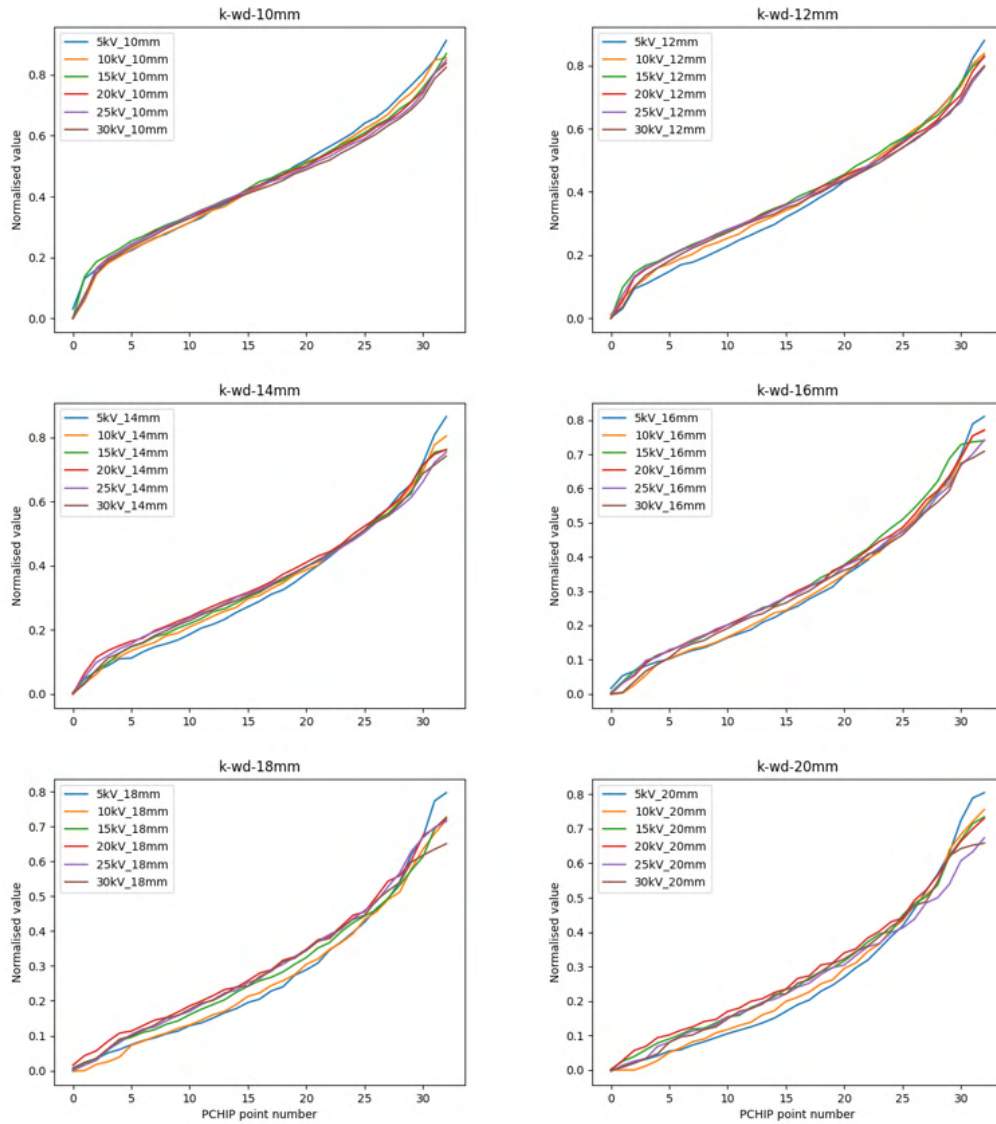Graphs of the parameter *b* dependent on the electron energy are shownn in Figure A.4.

Figure A.4: Graphs of the fitted *b* parameter grouped according to the same working distance.

The data show no clear dependency on electron energy.

Dependency on the working distance

The dependency of the parameter *b* on the working distance can be seen in Figure A.5.

Figure A.5: Graphs of the fitted b parameter grouped according to the same energy.

The graphs show clear dependency on the working distance. Similarly to parameter a, the b parameter is dependent only on one variable; thus, the same approach can be chosen. Averaged data can be seen in Figure A.3. The algorithm described in Section A can be applied to this parameter too.
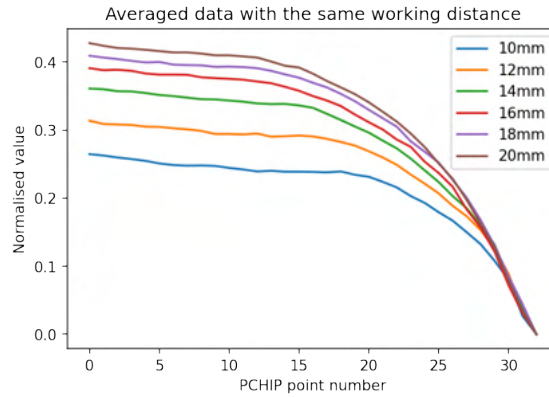
Figure A.6: Averaged data with the same working distance.

Parameter k

The case of the k parameter is very similar to that of the b parameter.

Dependecy on the electron energy

No clear dependecy has been spotted (Figure A.7)

Dependency on the working distance

The k parameter is dependent on the working distance (Figure A.8).

The last of the array parameters, k, can be approximated in the same way as the b parameter. The final graph is in Figure A.9 The algorithm is described in Section A.

Figure A.7: Graphs of the fitted k parameter grouped according to the same working distance. The data show no clear dependency on electron energy.
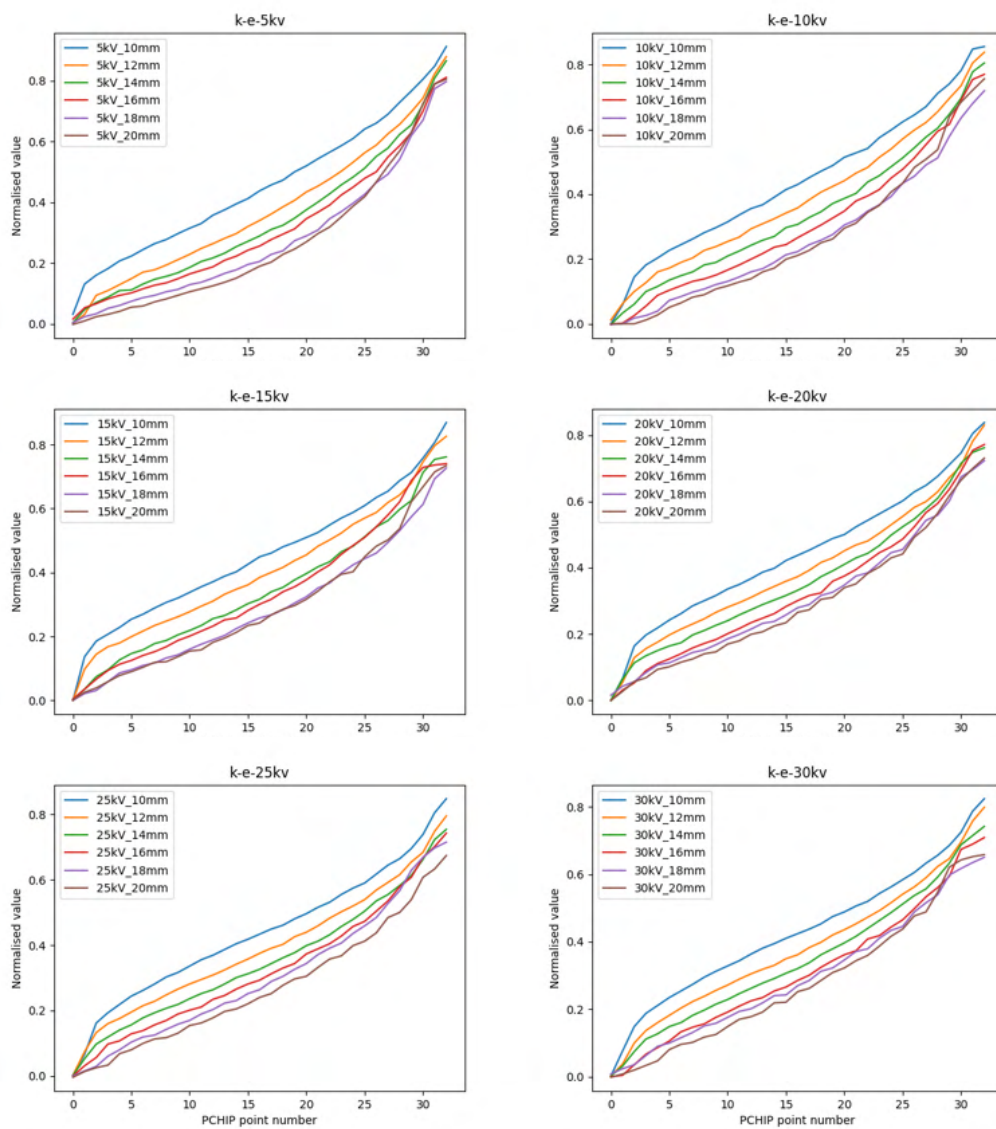
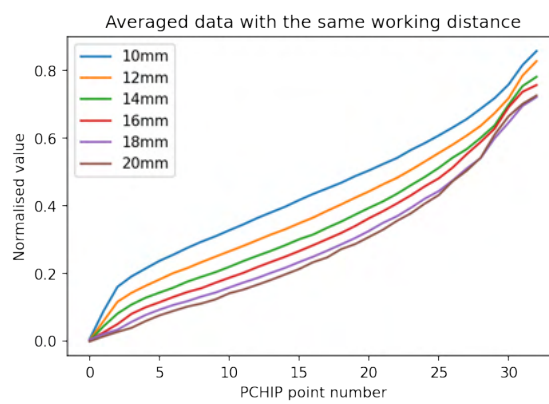Figure A.8: Graphs of the fitted k parameter grouped according to the same energy.

Figure A.9: Averaged data with the same working distance.

Approximating array parameters

All of the array parameters a, b, and k share the same principle of the approximation. Generally, it can be described as follows.

The parameter is defined by k sets of n points. This can be shown, for example, in Figure A.3, k is the number of plots, and n is the number of points in each of the plots. The whole dataset can be described as a matrix M with k columns and n rows. The matrix M is filled with k column vectors v_i, where the vector v_i represents n points of the $i-th$ set of points. It is important to keep the order of the sets that is defined by the relevant value for which it was measured (energy/working distance). After the matrix M was assembled, the final approximation of the parameter can be described as follows.

1. For each row of the matrix M, a PCHIP is created.

2. For every created PCHIP, a single value is retrieved at the point defined by the current energy/working distance value (energy for the a parameter, working distance otherwise).

3. A new PCHIP is created from the retrieved values. Because this PCHIP approximates the parameter with respect to the pixel value, it must be defined in the range <0,256>.

This new PCHIP approximates the required curve. By retrieving the value at the point specified by pixel intensity, a required parameter is obtained.

Parameter c

The c parameter is the scalar parameter, as there is no dependency on the pixel intensity. The results of fitting were very inconclusive, oscillating between 1.6 and 2.5. For each fitted superellipse, an average value was extracted, making it a scalar variable. The graphs of the different superellipses sorted by working distances and energies can be found in Figure A.10.
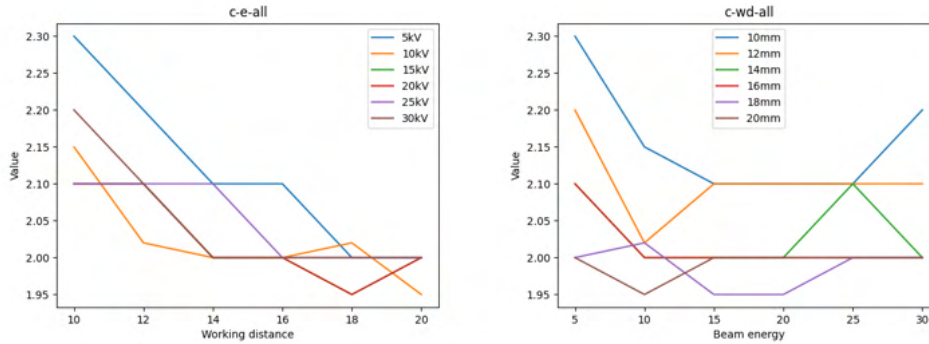

Figure A.10: The c parameter sorted by working distances and energies.

As no clear relation could be extracted from the data, a constant 2.1 was used.

Region of interest (Boundaries of the histogram)

In order to understand the estimation of boundaries, the influence of the beam current has to be understood first. As nowhere in the literature have been found any mentions about the electron current influencing the angular distribution of the backscattered electrons, it was assumed that its influence is restricted to the number of backscattered electrons. Because of this, it was expected that the influence of the electron current would be similar to the influence of the gain or the offset.

Influence of the beam current

Because the backscattering coefficient should not change, the bigger the electron current is supplied, the more electrons should become backscattered. The relationship was investigated, and the closest interpretation reached has shown that the influence can be simulated with the simple multiplication operation of an image (similar to gain). A few images acquired with different electron currents were analysed. The images were modified using the equation

$$n_{i,j} = p_{i,j} * \frac{I_t}{I_a} \tag{A.1}$$

where $p_{(}i,j)$ is pixel value at the i-th row and j-th column, $n_{(}i,j)$ is new pixel value at the coordinates, I_t is target current and I_a is acquisition current. Example of the transformation between currents can be seen at Figure A.13, which is histogram of transformed images from A.11. A histogram of images before the transformation can be seen in Figure A.12.
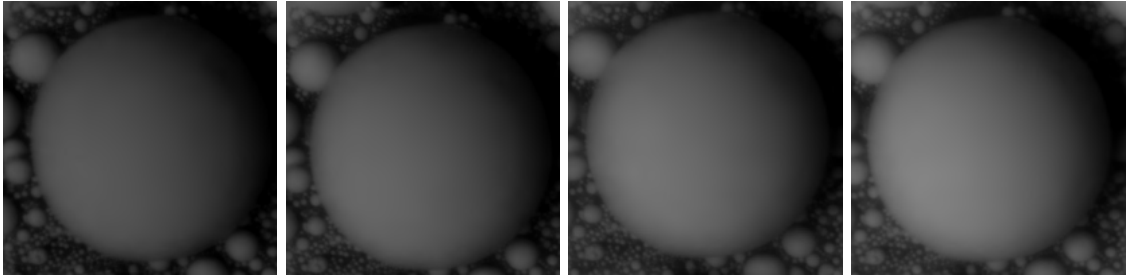

Figure A.11: Images acquired with the single segment of the 4Q BSE detector at electron currents of 7nA, 8nA, 9nA, and 10nA from left to right.
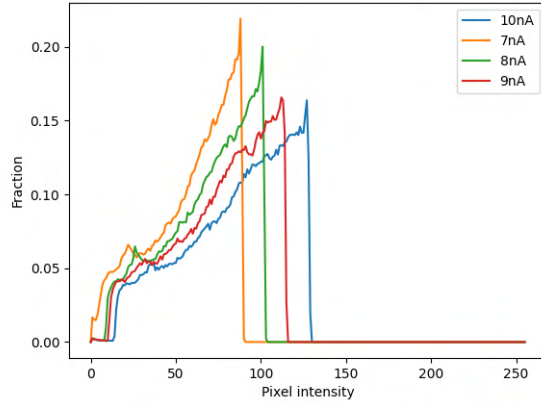
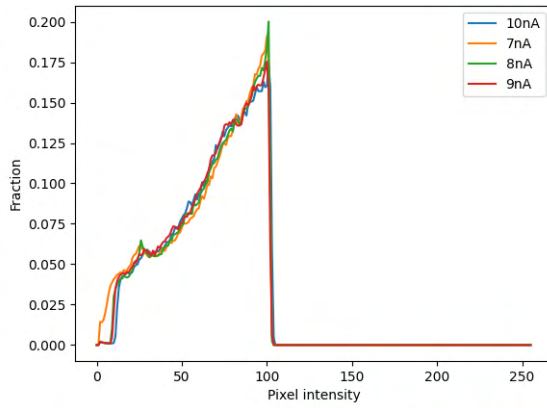Figure A.12: Overlayed histograms of the images from Figure A.11

Figure A.13: Overlayed histograms compensated for the current of 8nA.

Relations

With Equation A.1, the measured borders of interest have been transformed to represent the acquisition at 5nA. The resulting graphs are shown in Figure A.14

It can be seen that the dependency on various energies is approximately linear. For simplicity, a linear function has been fitted to approximate this relation.

It must be noted that this approximation is created for the current of 5nA. For transformation to the different electron current, Equation A.1 must be used.
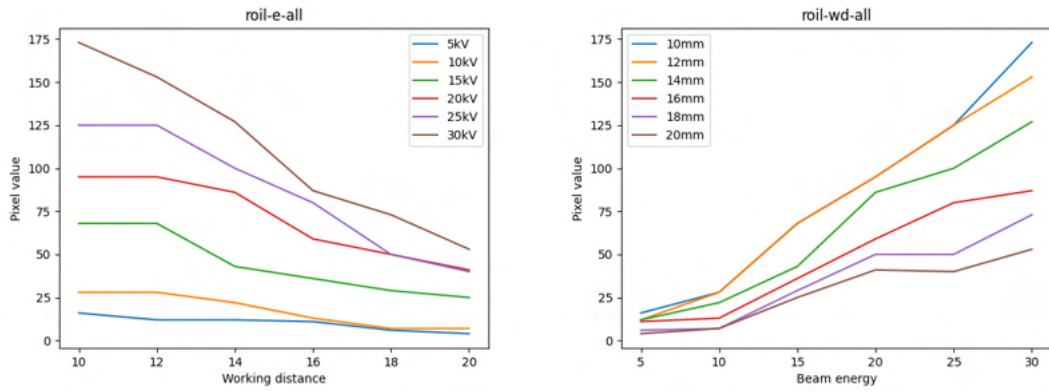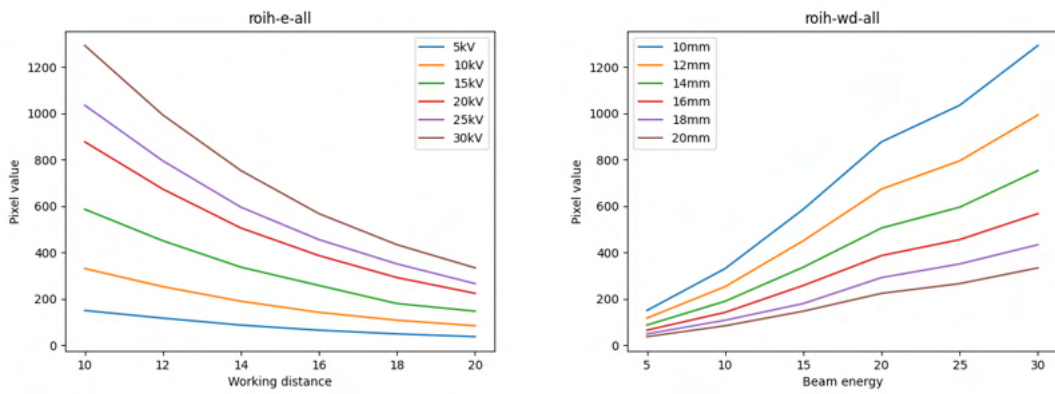
Figure A.14: Lower boundary
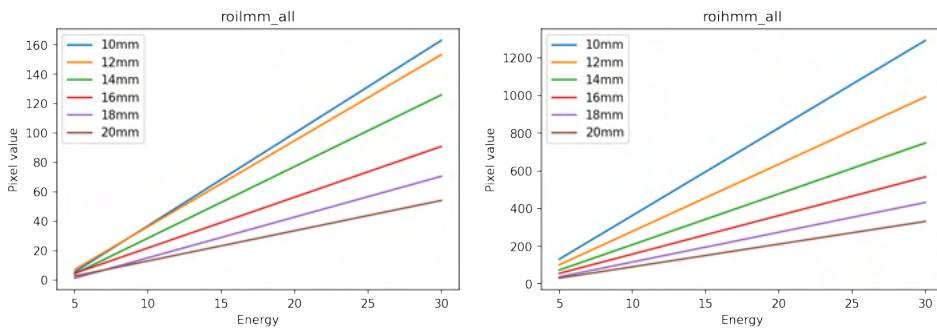

Figure A.15: Upper boundary

Figure A.16: Fitted function as relation of energy to the pixel intensity.